Supplementary Information (SI) for Inorganic Chemistry Frontiers.

Supporting Information

A Hybrid Pyridine-Thioether Macrocycle to Chelate Theranostic Copper and Silver Radioisotopes

Marianna Tosato[1,2,*], Fortuna Ponte[3], Sara Franchi[4], Nora V. May[5], Mikael Jensen[6], Helmut Mäcke[7], Valerio Di Marco[4], Laura Pigani[8], Erika Ferrari[8], Emilia Sicilia[3], Mattia Asti[9] and Caterina F. Ramogida[1,2,*]

[1] Department of Chemistry, Simon Fraser University, V5A 4Y8 Burnaby, British Columbia, Canada
[2] Life Sciences, TRIUMF, V6T 2A3 Vancouver, British Columbia, Canada
[3] Department of Chemistry and Chemical Technologies, University of Calabria, 87036 Cosenza, Italy
[4] Department of Chemical Sciences, University of Padova, 35131 Padova, Italy
[5] Centre for Structural Science, Research Centre for Natural Sciences, 1117 Budapest, Hungary
[6] The Hevesy Laboratory, Department of Health Technology, Technical University of Denmark, 4000 Roskilde, Denmark
[7] Department of Nuclear Medicine, University Hospital Freiburg, D-79106 Freiburg, Germany
[8] Department of Chemical and Geological Sciences, University of Modena and Reggio Emilia, 41125 Modena, Italy
[9] Radiopharmaceutical Chemistry Laboratory, Nuclear Medicine Unit, AUSL-IRCCS Reggio Emilia, 42122 Reggio Emilia, Italy

Corresponding authors: marianna_tosato@sfu.ca; cfr@sfu.ca

Supporting Figures

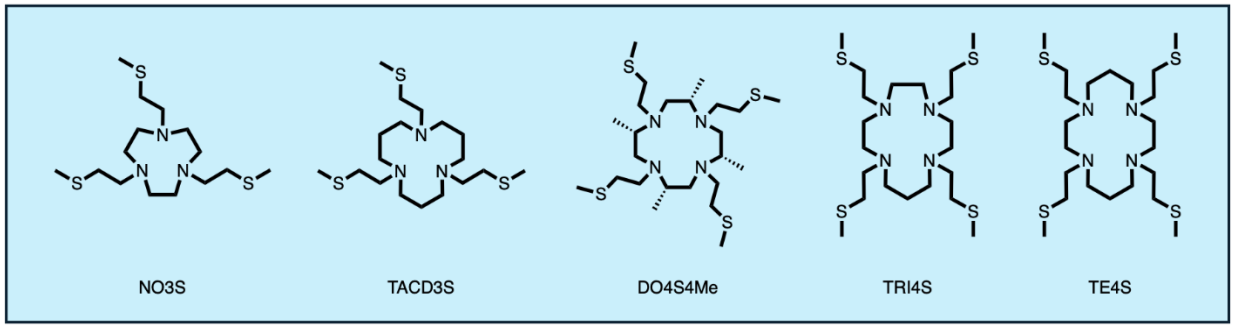

Figure S1. Chemical structures of previously developed sulfur-containing chelators for soft radiometals characterized by different ring topologies.[1,2]

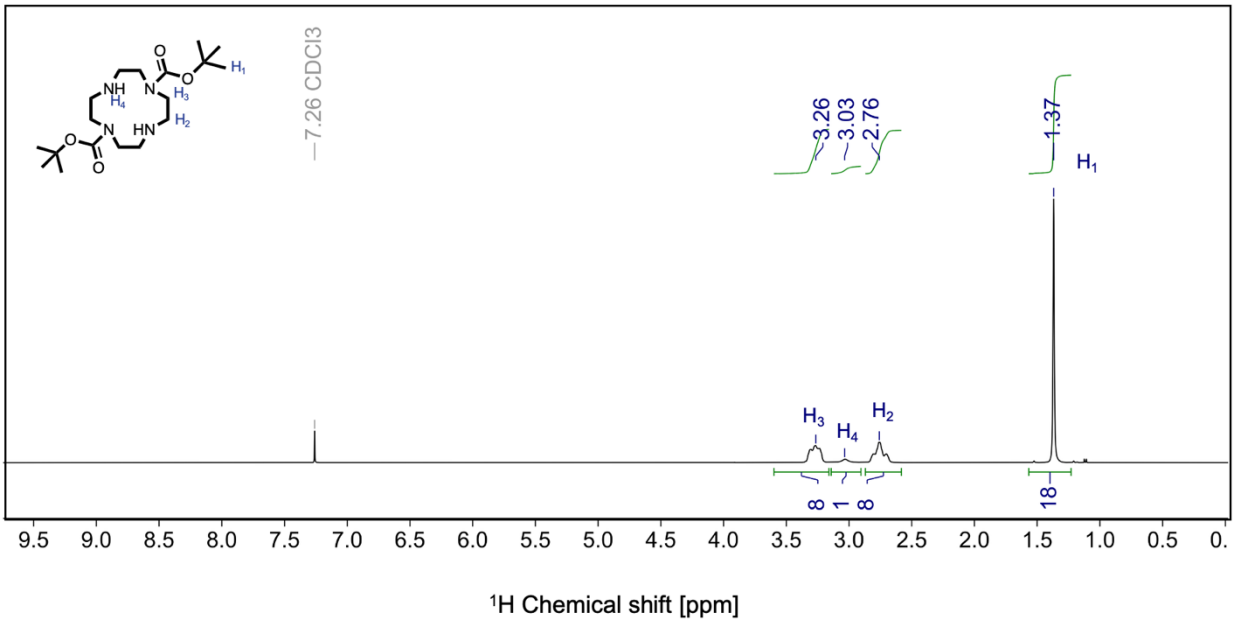

Figure S2. ^{1}H NMR spectrum of 1,7-bis(tert-butyloxycarbonyl)-1,4,7,10-tetraazacyclododecane - di-Boc-cyclen (400 MHz, $CDCl_3$, T = 25°C) and signal attributions.

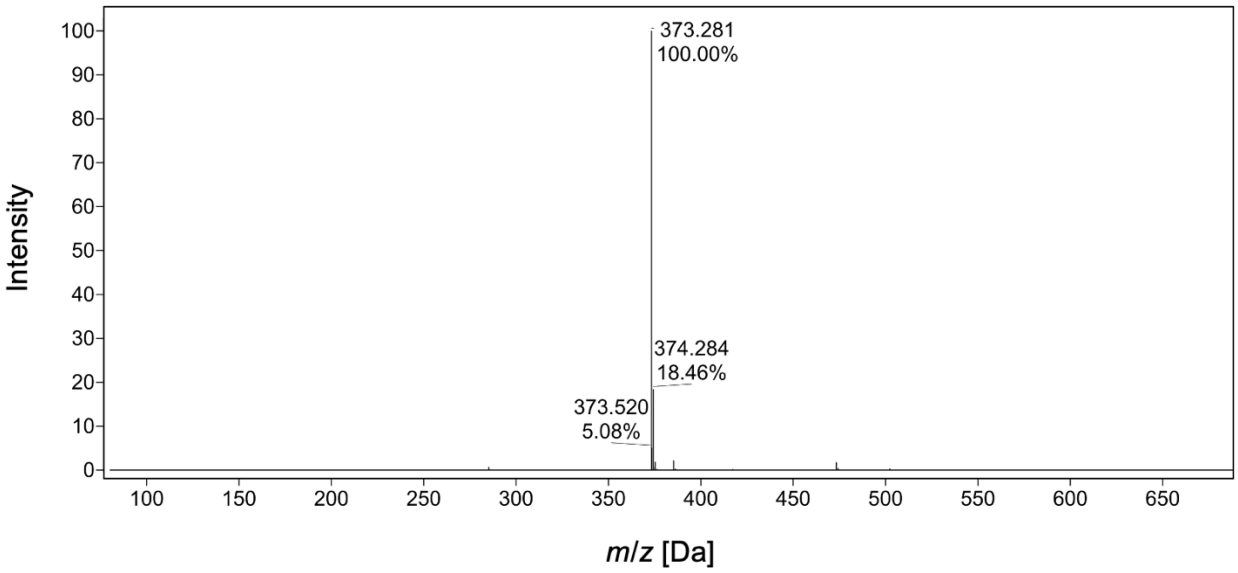

Figure S3. HR-MS spectrum of [di-Boc-cyclen-H]$^+$.

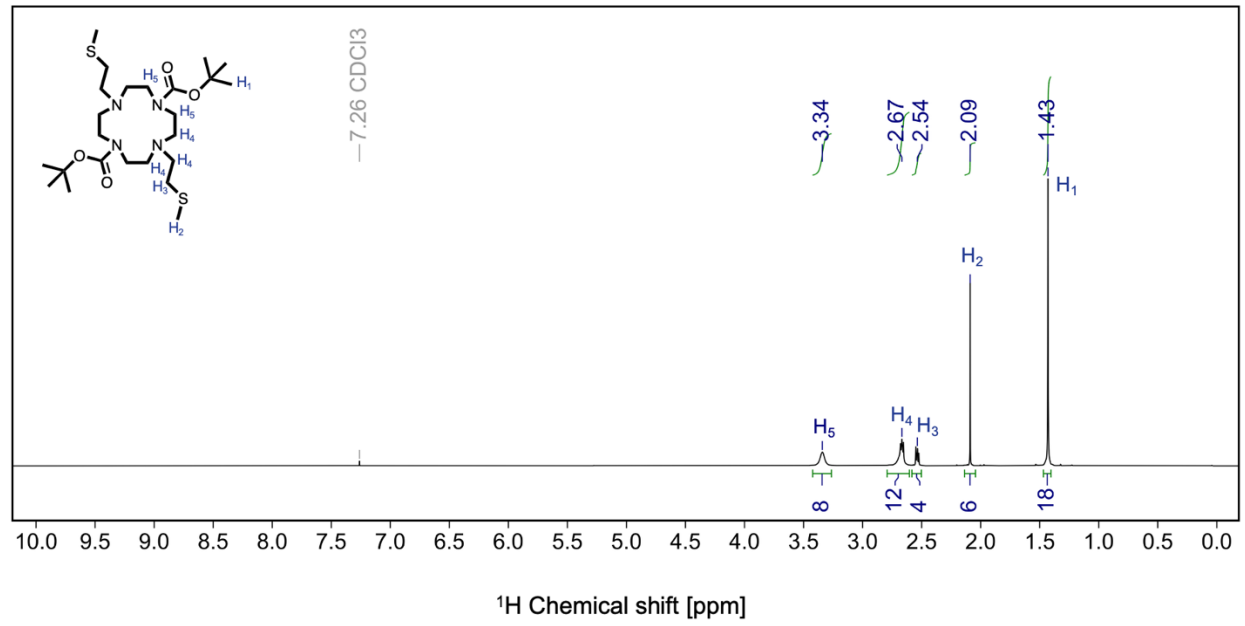

Figure S4. ^{1}H NMR spectrum of 1,7-bis(tert-butyloxycarbonyl)-4,10-bis(2-(methylsulfanyl)ethyl)-1,4,7,10-tetraazacyclododecane - di-Boc-DO2S (400 MHz, $CDCl_3$, *T* = 25°C) and signal attributions.

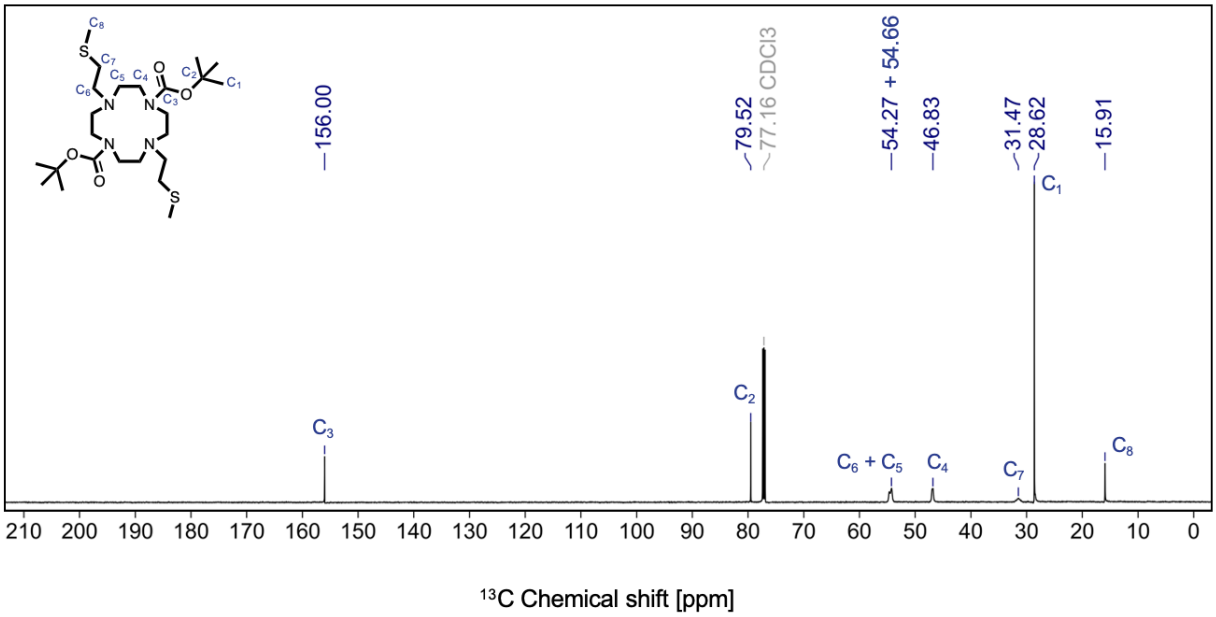

Figure S5. $^{13}C\{^{1}H\}$ NMR spectrum of di-Boc-DO2S (400 MHz, $CDCl_3$, *T* = 25°C) and signal attributions.

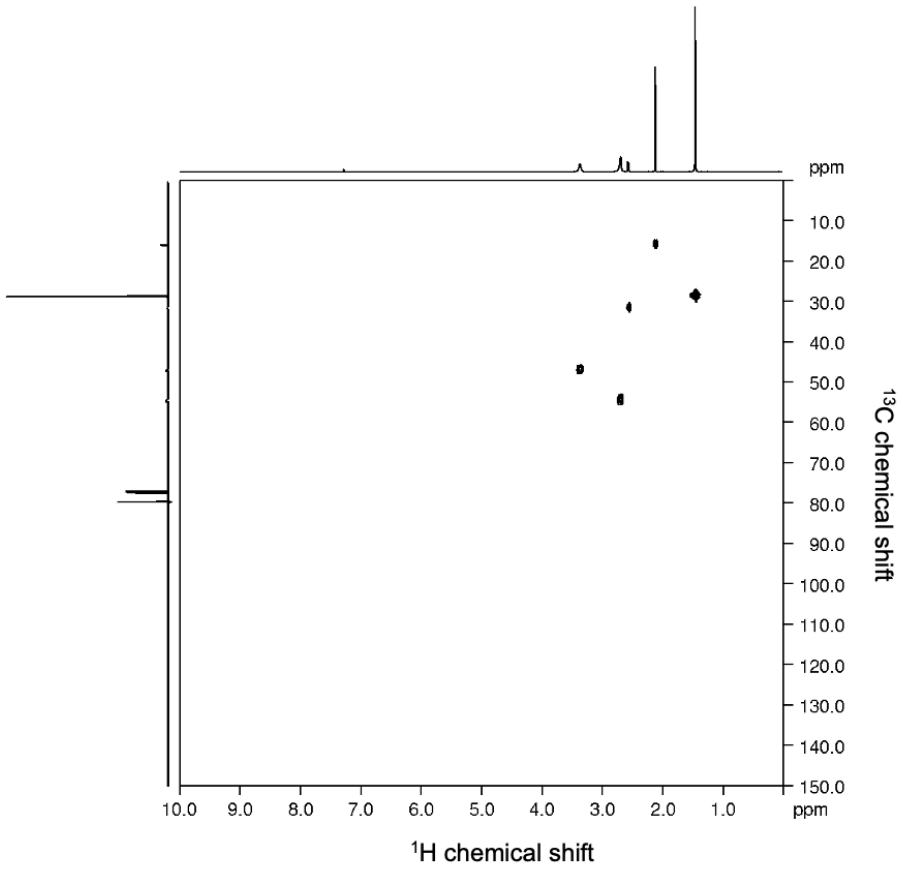

Figure S6. ^{1}H-^{13}C HSQC spectrum of di-Boc-DO2S (400 MHz, $CDCl_3$, T = 25°C).

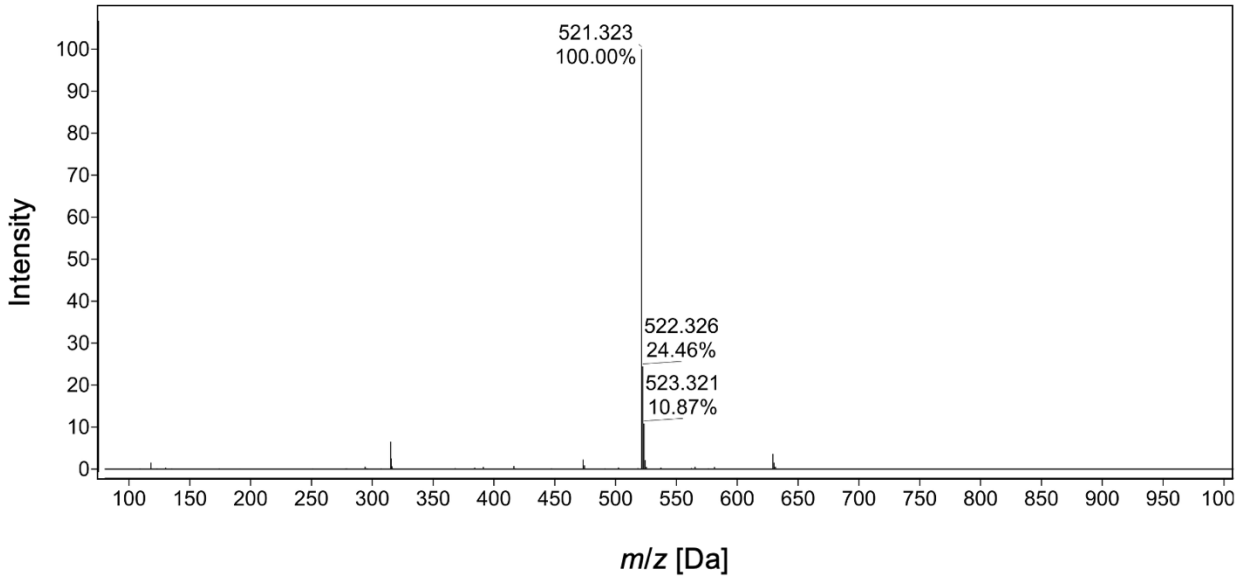

Figure S7. HR-MS spectrum of [di-Boc-DO2S-H]$^{+}$.

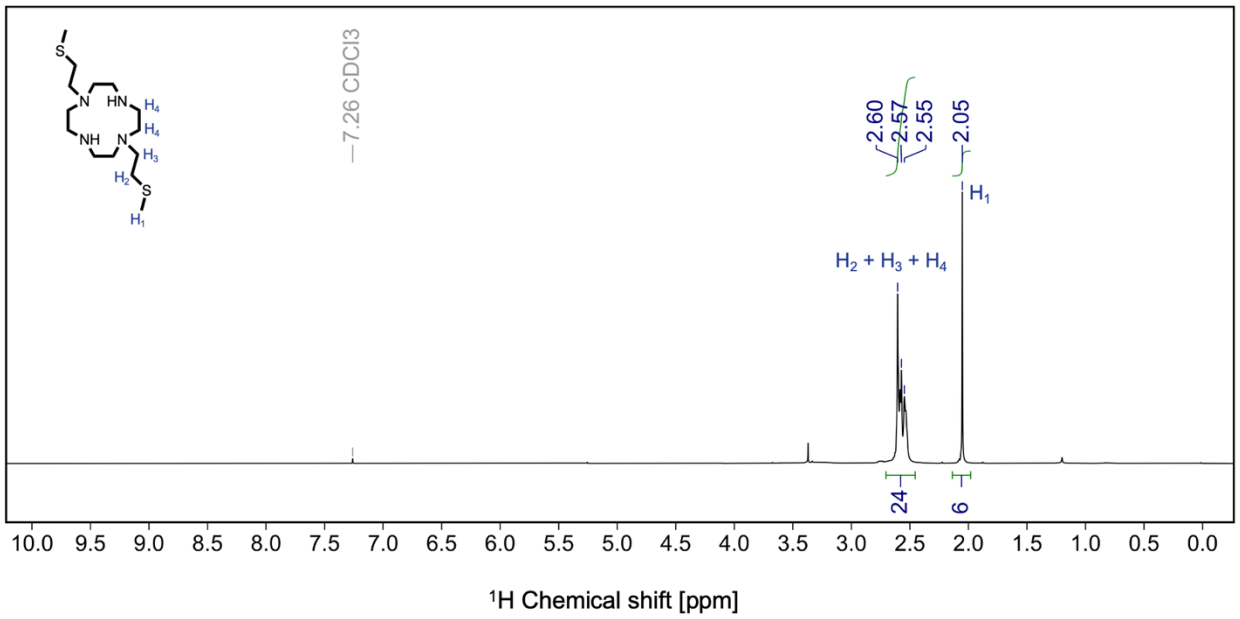

Figure S8. ^{1}H NMR spectrum of 1,7-bis(2-(methylsulfanyl)ethyl)-1,4,7,10-tetraazacyclododecane - DO2S (400 MHz, $CDCl_3$, T = 25°C) and signal attributions.

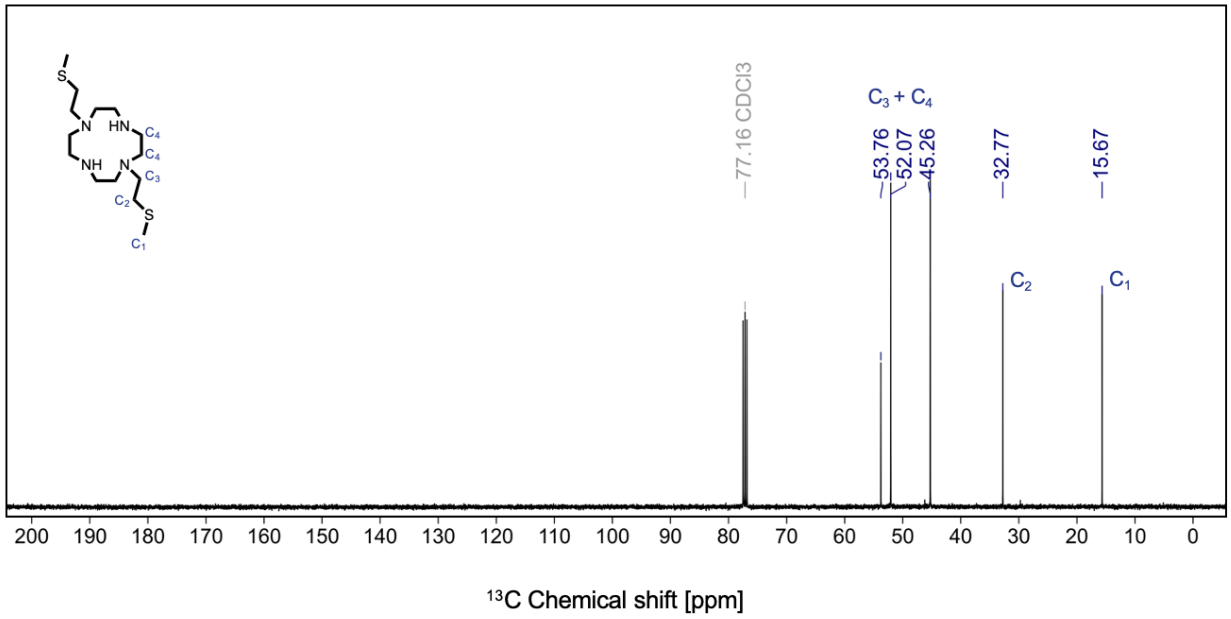

Figure S9. $^{13}C\{^{1}H\}$ NMR spectrum of DO2S (400 MHz, $CDCl_3$, T = 25°C) and signal attributions.

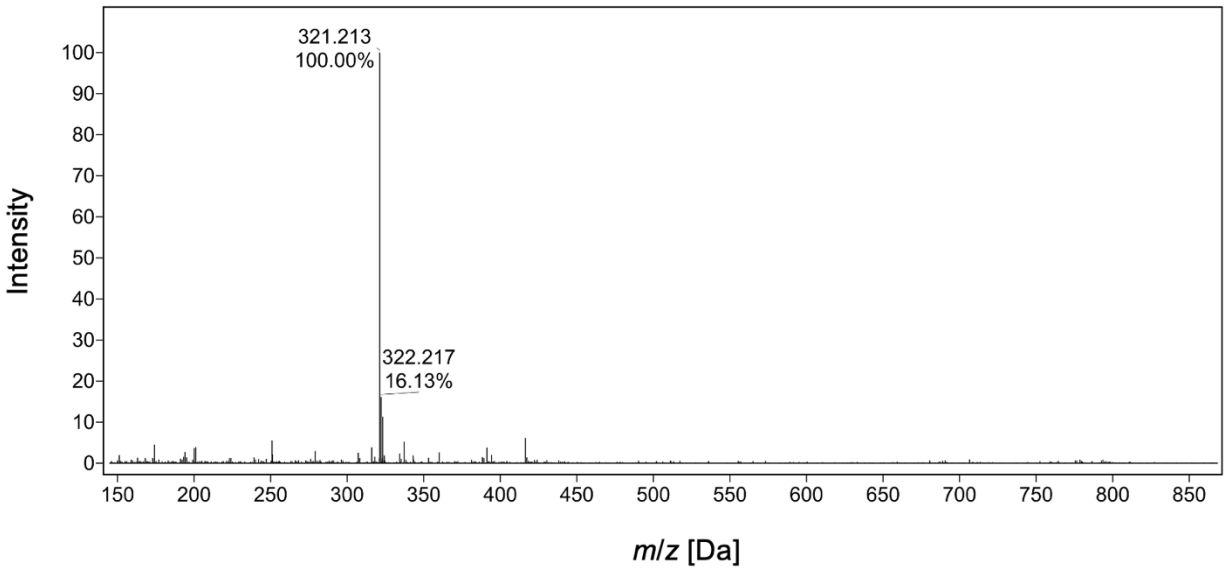

Figure S10. HR-MS spectrum of $[DO2S-H]^+$.

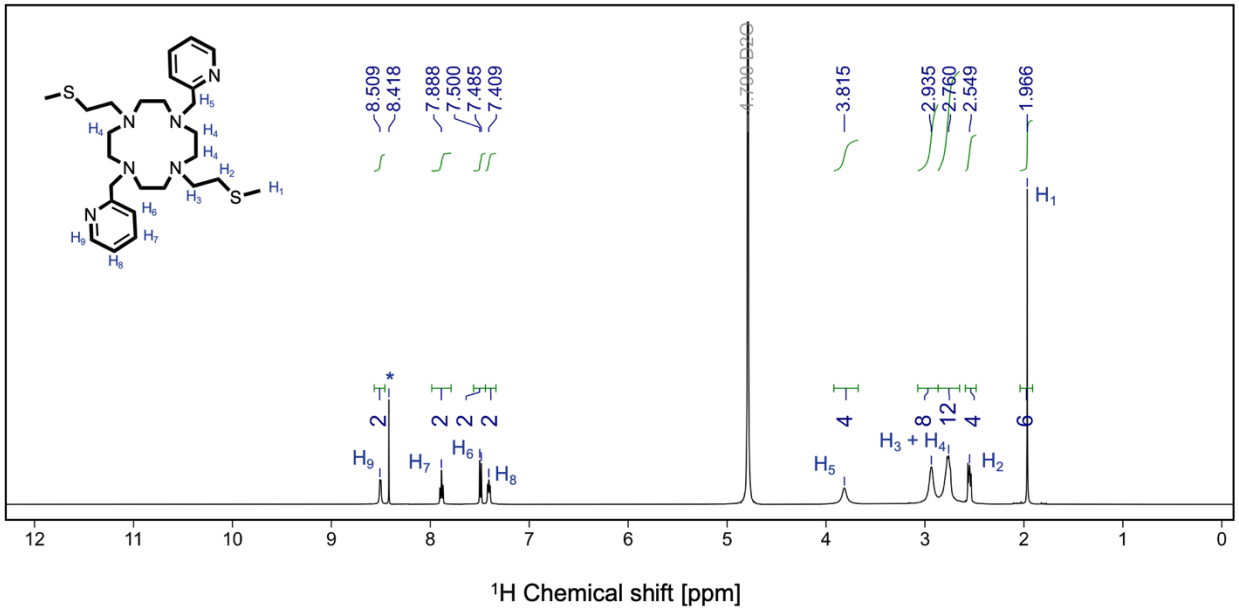

Figure S11. ^{1}H NMR spectrum of 1,7-bis(2-(methylsulfanyl)ethyl)-4,10- bis(pyridin-2-ylmethyl)-1,4,7,10-tetraazacyclododecane - DO2S2Py (400 MHz, D_2O, T = 25°C) and signal attributions. The peak indicated with an asterisk is related to residual formic acid.

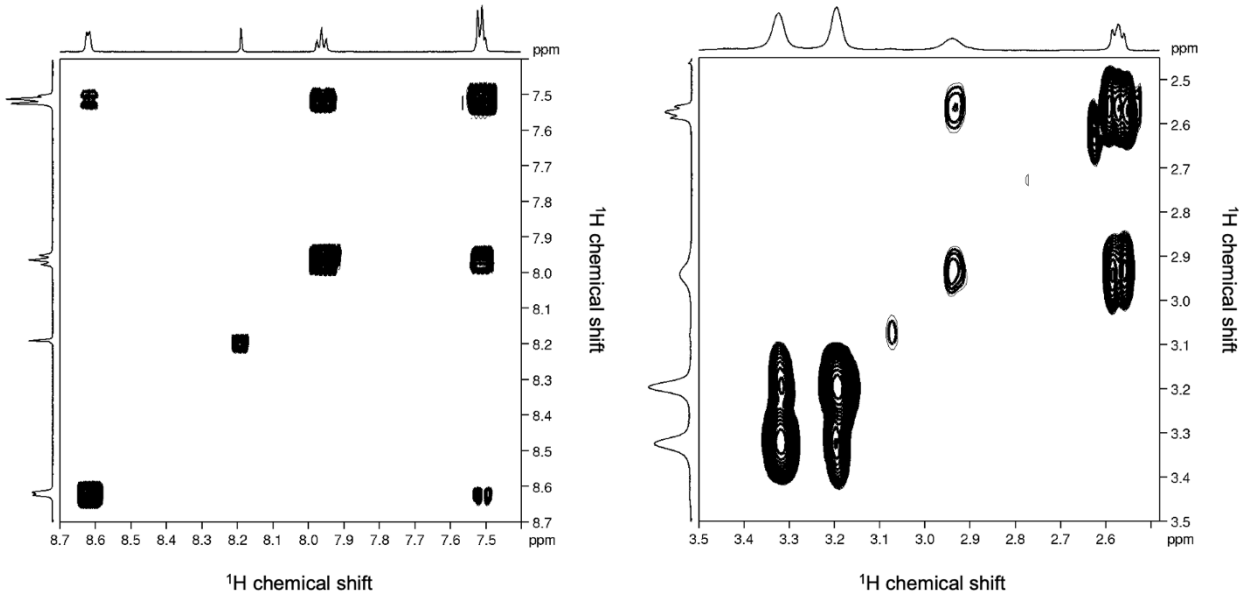

Figure S12. ^{1}H-^{1}H COSY spectrum of DO2S2Py (400 MHz, D_2O, T = 25°C, pD ~ 3).

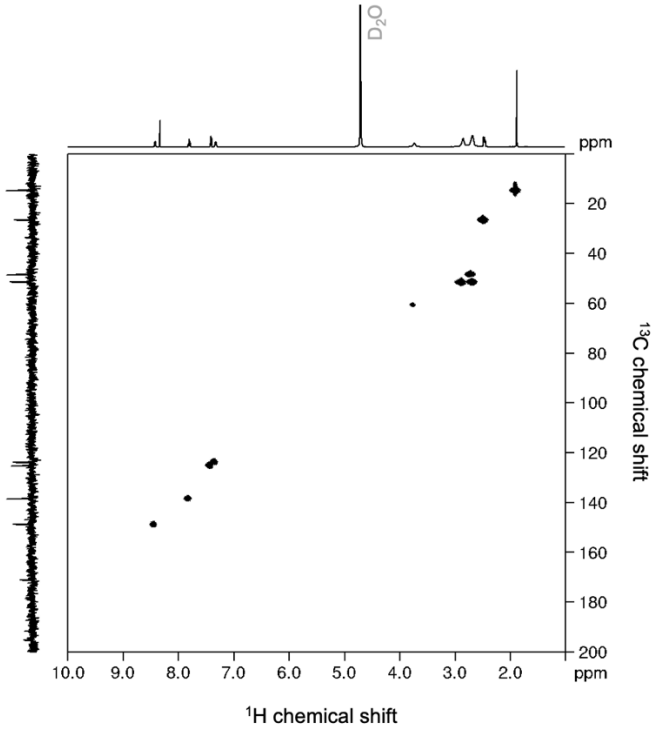

Figure S13. ^{1}H-^{13}C HSQC spectra of DO2S2Py (400 MHz, D_2O, T = 25°C, pD ~ 9).

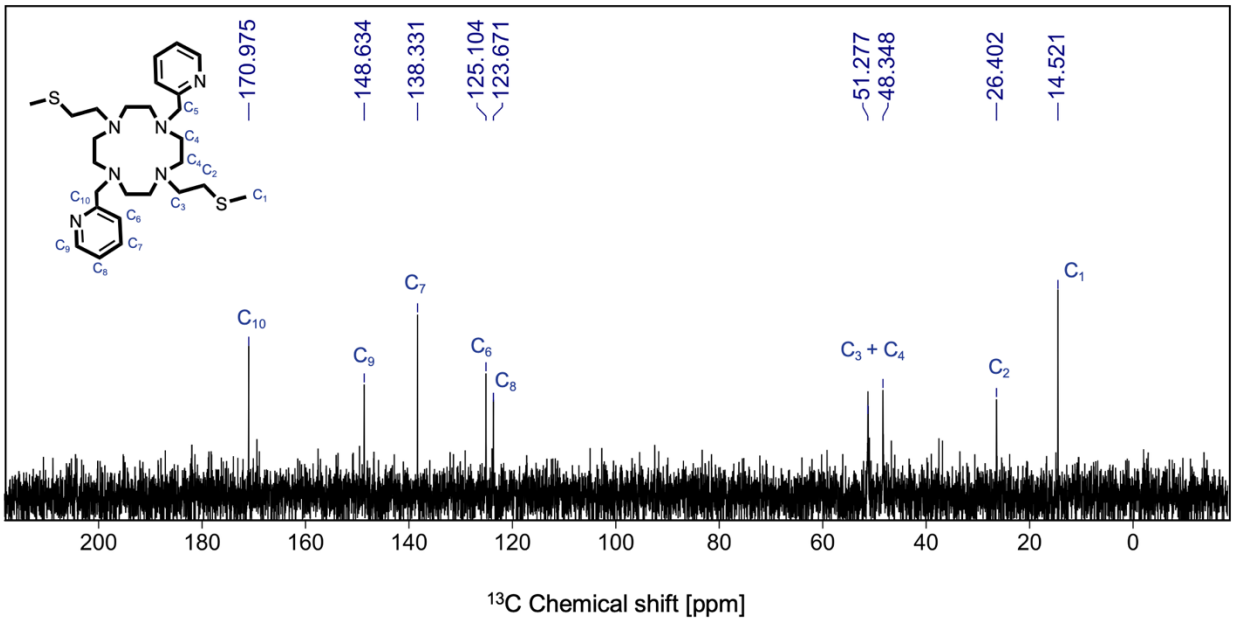

Figure S14. $^{13}C\{^{1}H\}$ NMR spectrum of DO2S2Py (400 MHz, D_2O, *T* = 25°C) and signal attributions.

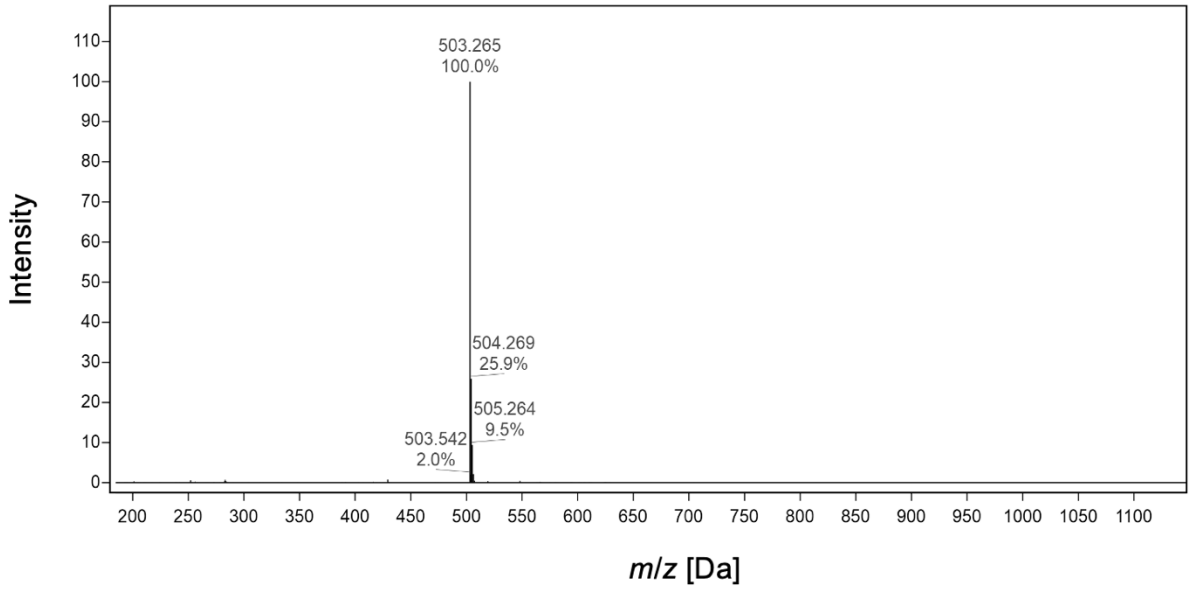

Figure S15. HR-MS spectrum of $[DO2S2Py\text{-}H]^+$.

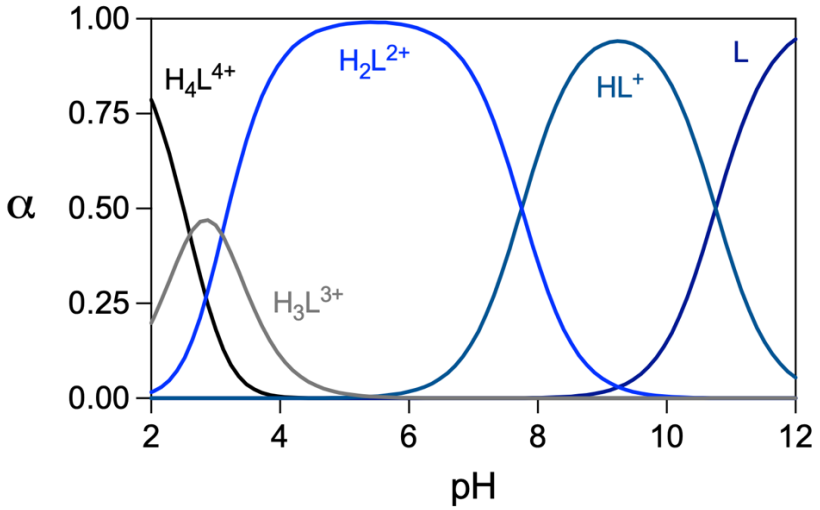

Figure S16. Distribution diagram of DO2S2Py, where α represent the ratio between the concentration of a given protonation state and the total concentration of all species at equilibrium.

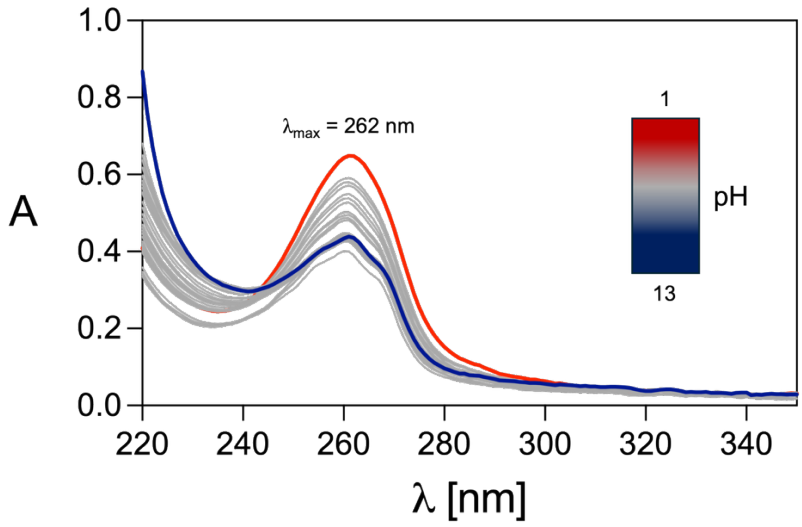

Figure S17. UV-Vis spectra of DO2S2Py at different pH values (T = 25°C, I = 0.1 M NaCl, $C_{DO2S2Py}$ = $1 \cdot 10^{-4}$ M).

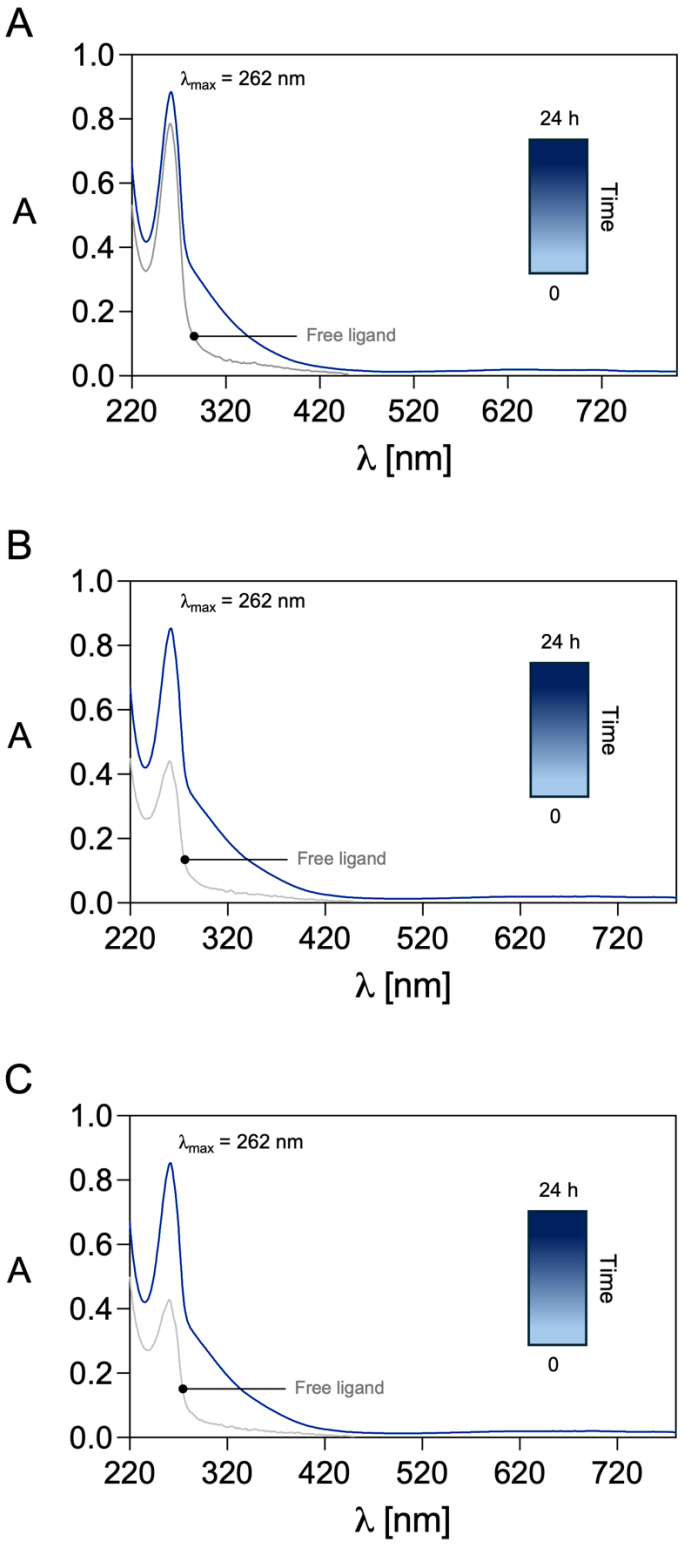

Figure S18. Representative time-dependent UV-Vis spectra of Cu^{2+}-DO2S2Py mixtures at pH (A) 2 (B) 4.5, and (C) pH 6.8 (T = 25°C, I = 0.15 M NaCl, $C_{DO2S2Py}$ = C_{Cu} = $1 \cdot 10^{-4}$ M). No spectral variations were observed over time nor after extended heating.

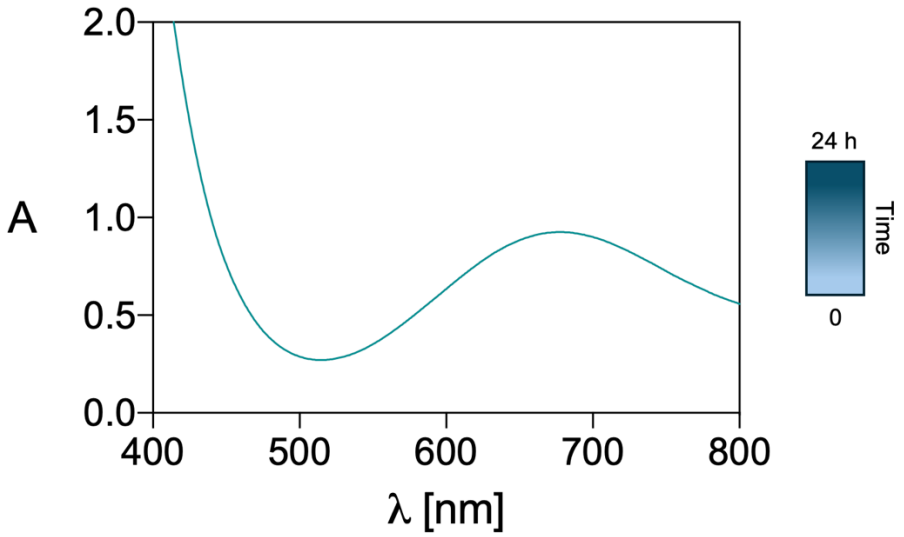

Figure S19. Representative time-dependent UV-Vis spectra of Cu^{2+}-DO2S2Py (T = 25°C, I = 0.15 M NaCl, $C_{DO2S2Py}$ = C_{Cu} = $1 \cdot 10^{-3}$ M, pH 4.5). No spectral variations were observed over time nor after extended heating. Free DO2S2Py shows no absorption in the reported spectral region.

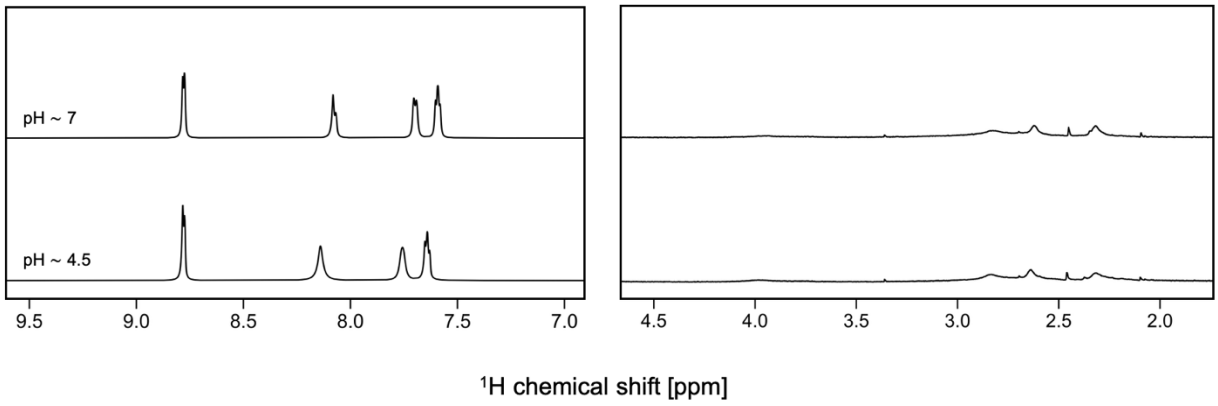

Figure S20. Representative ^{1}H NMR spectra of Ag^+-DO2S2Py mixtures at different pH (400 MHz, D_2O, T = 25°C, I = 0.15 M $NaNO_3$, $C_{DO2S2Py}$ = C_{Ag} =$1 \cdot 10^{-3}$ M). No spectral variations were observed over time nor after extended heating. The spectra of the free ligands are reported in **Figure 2**.

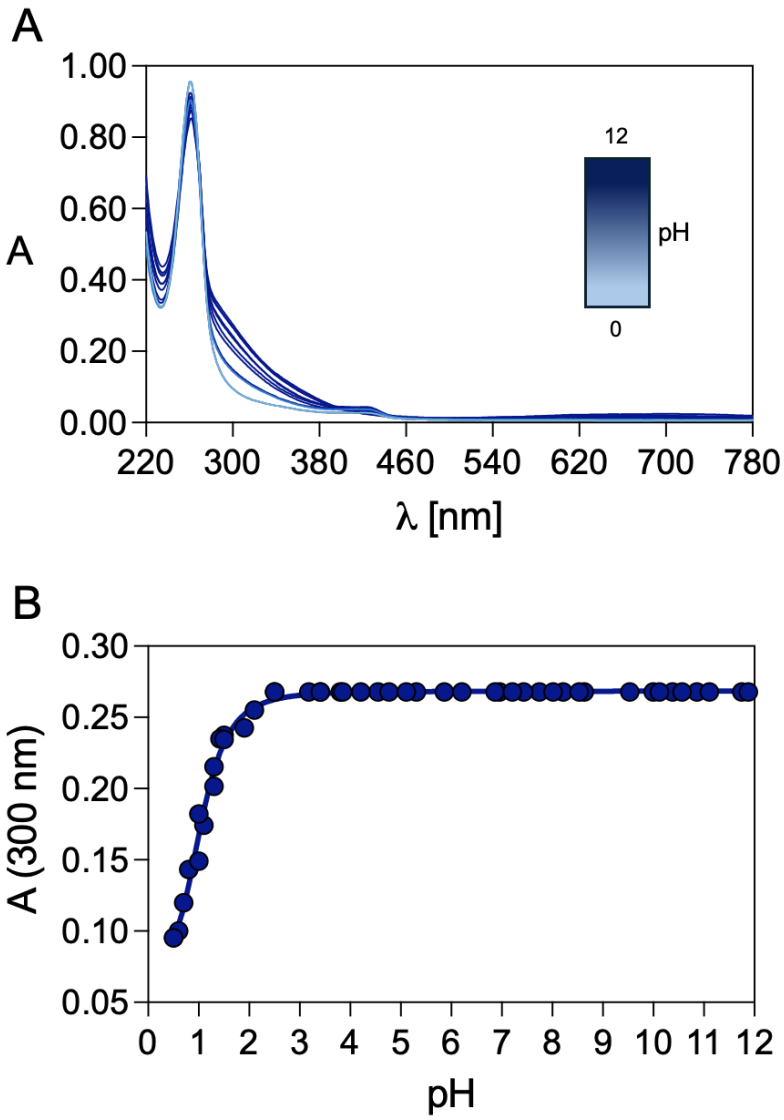

Figure S21. Representative (A) pH-dependent UV-Vis spectra of Cu^{2+}-DO2S2Py (T = 25°C, I = 0.15 M NaCl, $C_{DO2S2Py}$ = C_{Cu} = $1 \cdot 10^{-4}$ M) and (B) variation of absorbance at 300 nm as a function of pH.

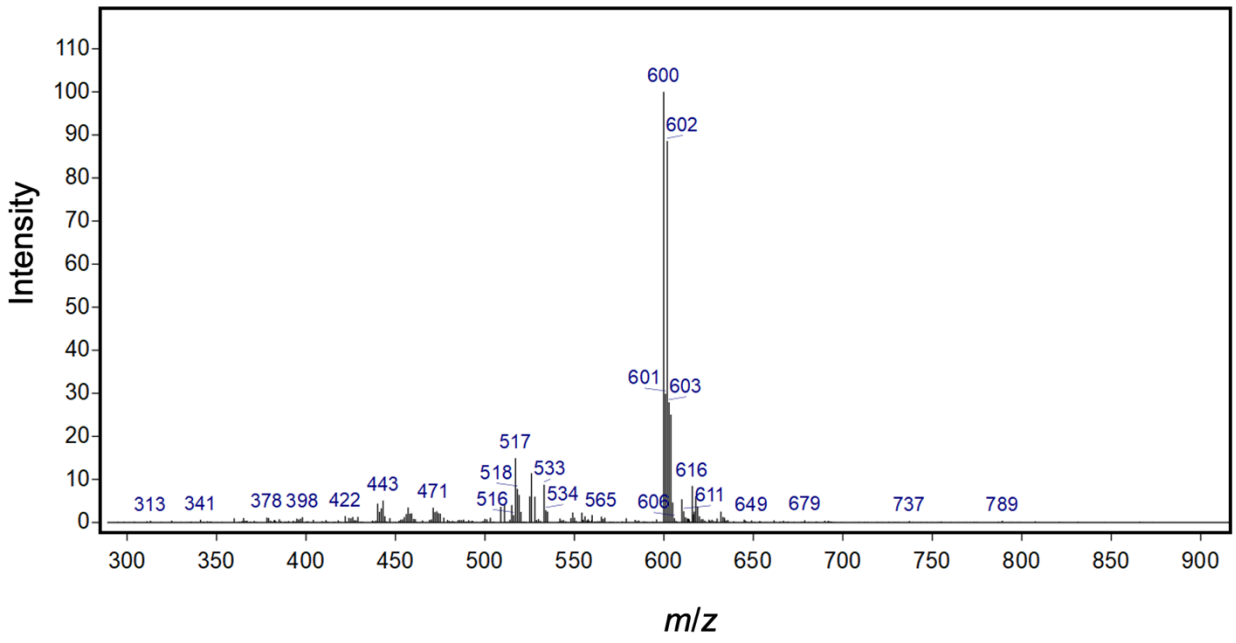

Figure S22. ESI-MS spectra of Cu^{2+}-DO2S2Py. The peak at *m*/*z* 600 corresponds to $[Cu(DO2S2Py)(Cl)]^+$ (calc. *m*/*z* 600.19 for $[C_{26}H_{42}ClCuN_6S_2]^+$).

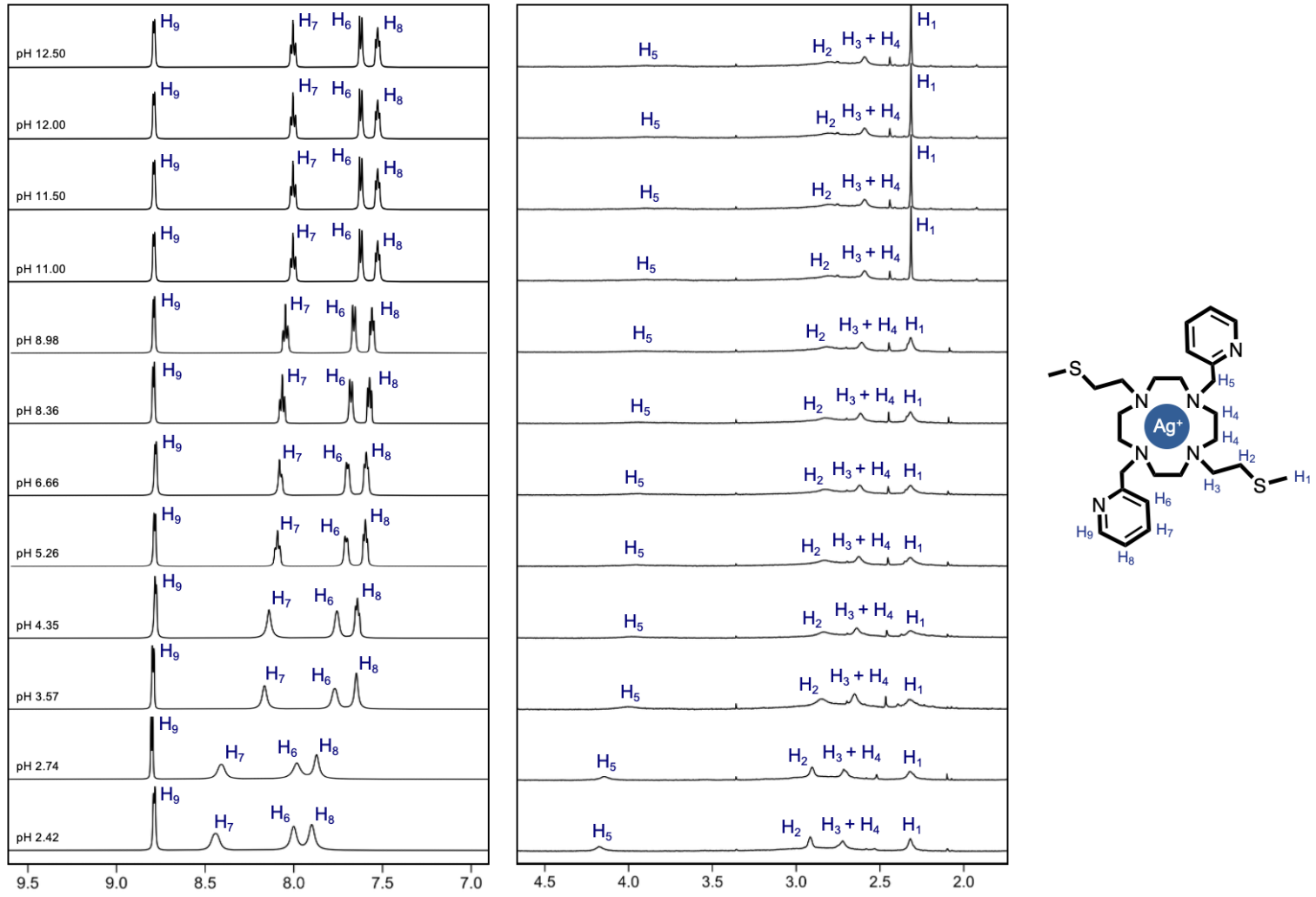
pH 12.50
pH 12.00
pH 11.50
pH 11.00
pH 8.98
pH 8.36
pH 6.66
pH 5.26
pH 4.35
pH 3.57
pH 2.74
pH 2.42
H9
H7
H6
H8
H5
H2
H3 + H4
H1
9.5
9.0
8.5
8.0
7.5
7.0
4.5
4.0
3.5
3.0
2.5
2.0
Ag+
N
S
H4
H3
H9
H8
[1]H chemical shift [ppm]

Figure S23. Representative ^{1}H NMR spectra of Ag^{+}-DO2S2Py at different pH (400 MHz, D_2O, T = 25°C, I = 0.15 M $NaNO_3$, $C_{DO2S2Py}$ = C_{Ag} = $1 \cdot 10^{-3}$ M) and signal attributions. Aromatic and aliphatic intensity scales are different.

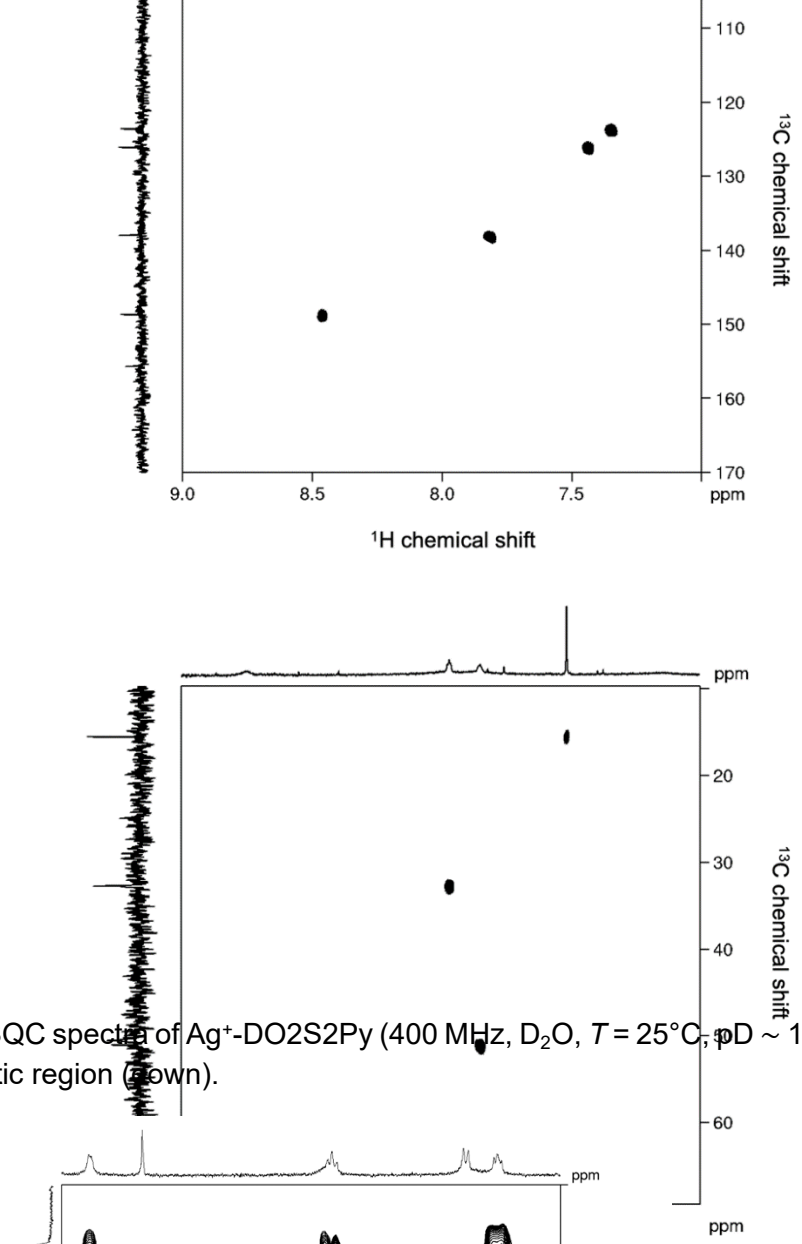

Figure S24. ^{1}H-^{13}C HSQC spectra of Ag^{+}-DO2S2Py (400 MHz, D_2O, T = 25°C, pD ~ 11): aromatic region (up) and aliphatic region (down).

Figure S25. ^{1}H-^{1}H COSY spectra (aromatic region) of Ag^{+}-DO2S2Py (400 MHz, D_2O, T = 25°C, pD ~ 11).

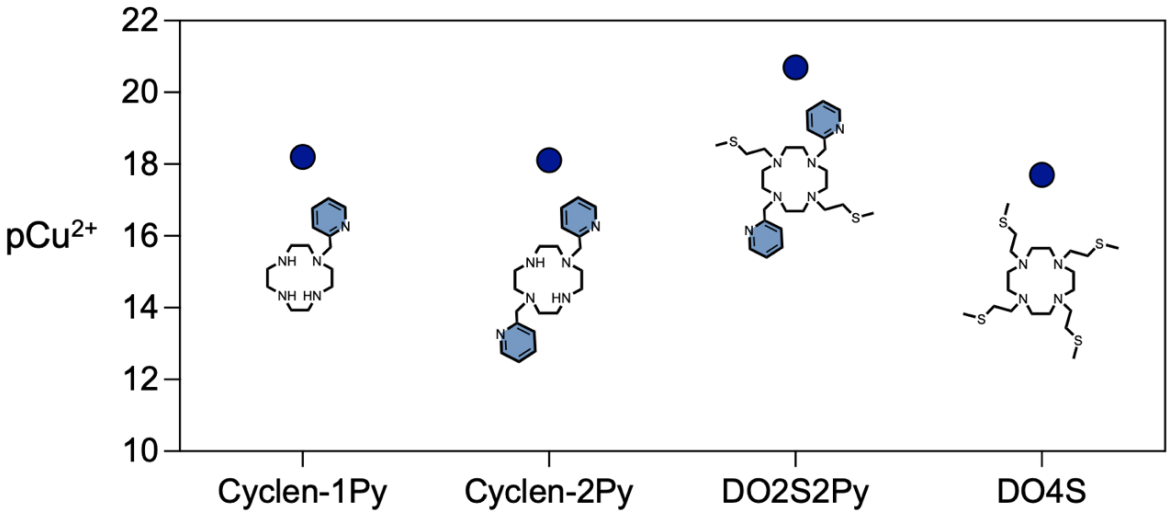

Figure S26. Comparison of pCu^{2+} values between DO2S2Py, DO4S and other py-containing chelators. pCu^{2+} were calculated at pH 7.4, $C_{DO2S2Py}$ = 1·10^{-5} M and C_{Cu} = 1·10^{-6} M.

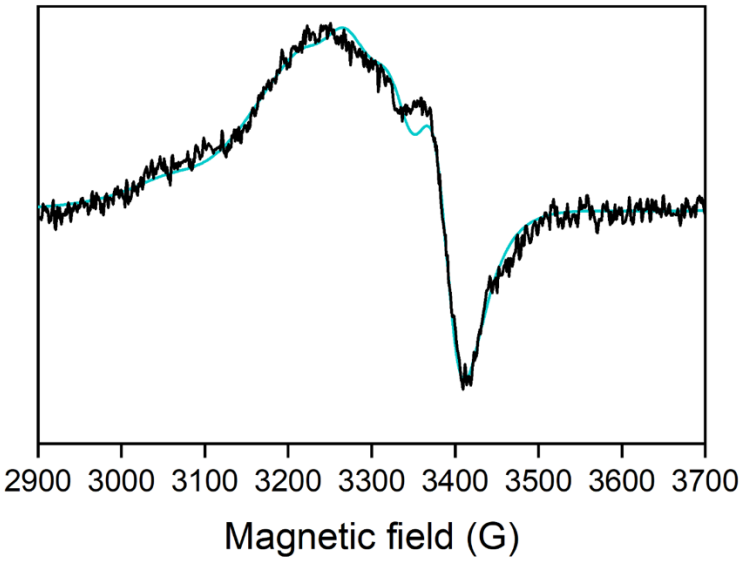

Figure S27. Measured (**black**) and simulated (**light blue**) room temperature EPR spectra of $[Cu(DO2S2Py)]^{2+}$. For the simulation, anisotropic EPR parameters were considered with a rotation correlation time of $4.2 \cdot 10^{-10}$ s.

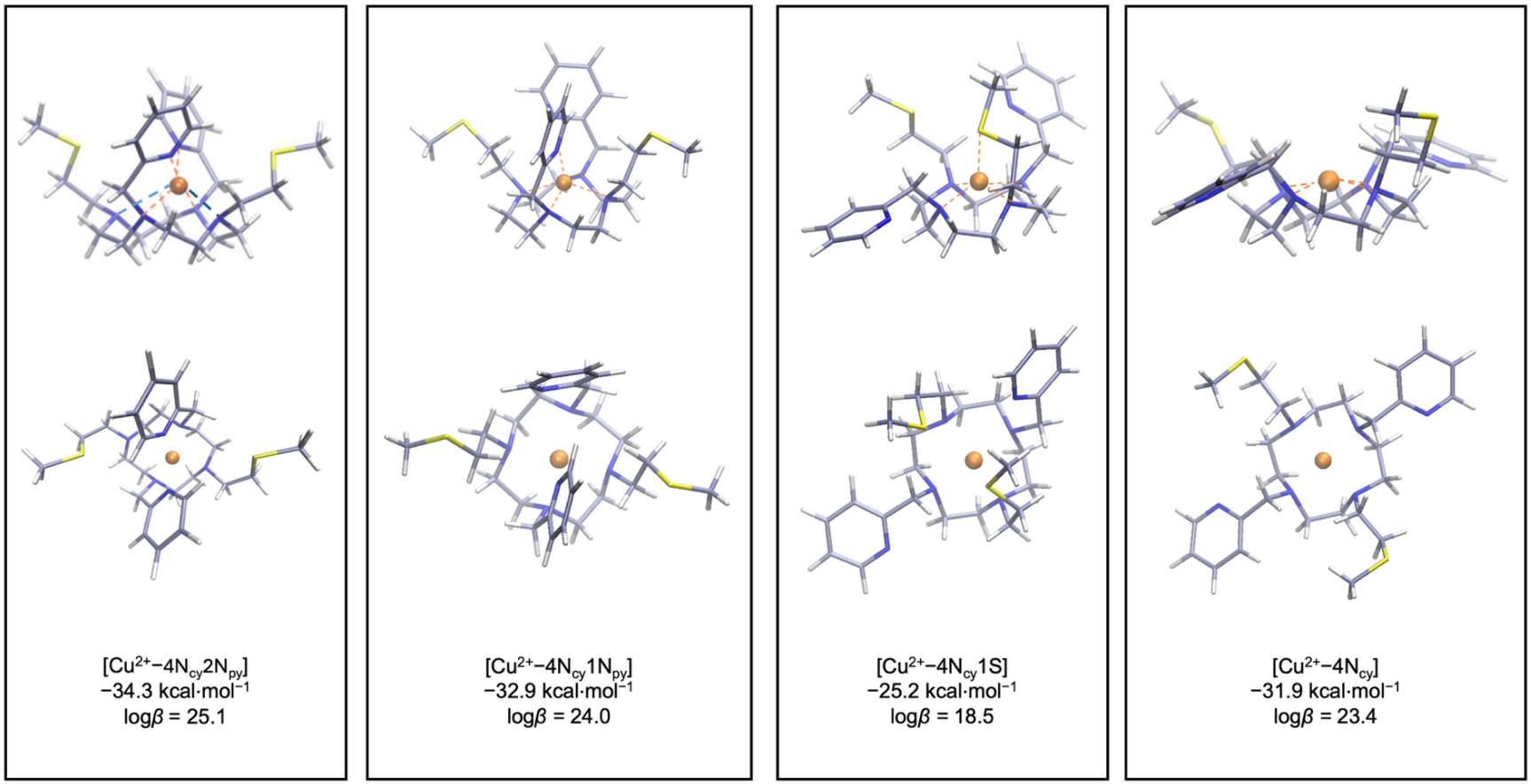

Figure S28. B3PW91 optimized geometrical structures of $[Cu(DO2S2Py)]^{2+}$ calculated in water together with the relative binding energies (kcal·mol^{-1}) and corresponding logβ values. Structures are displayed from multiple perspectives.

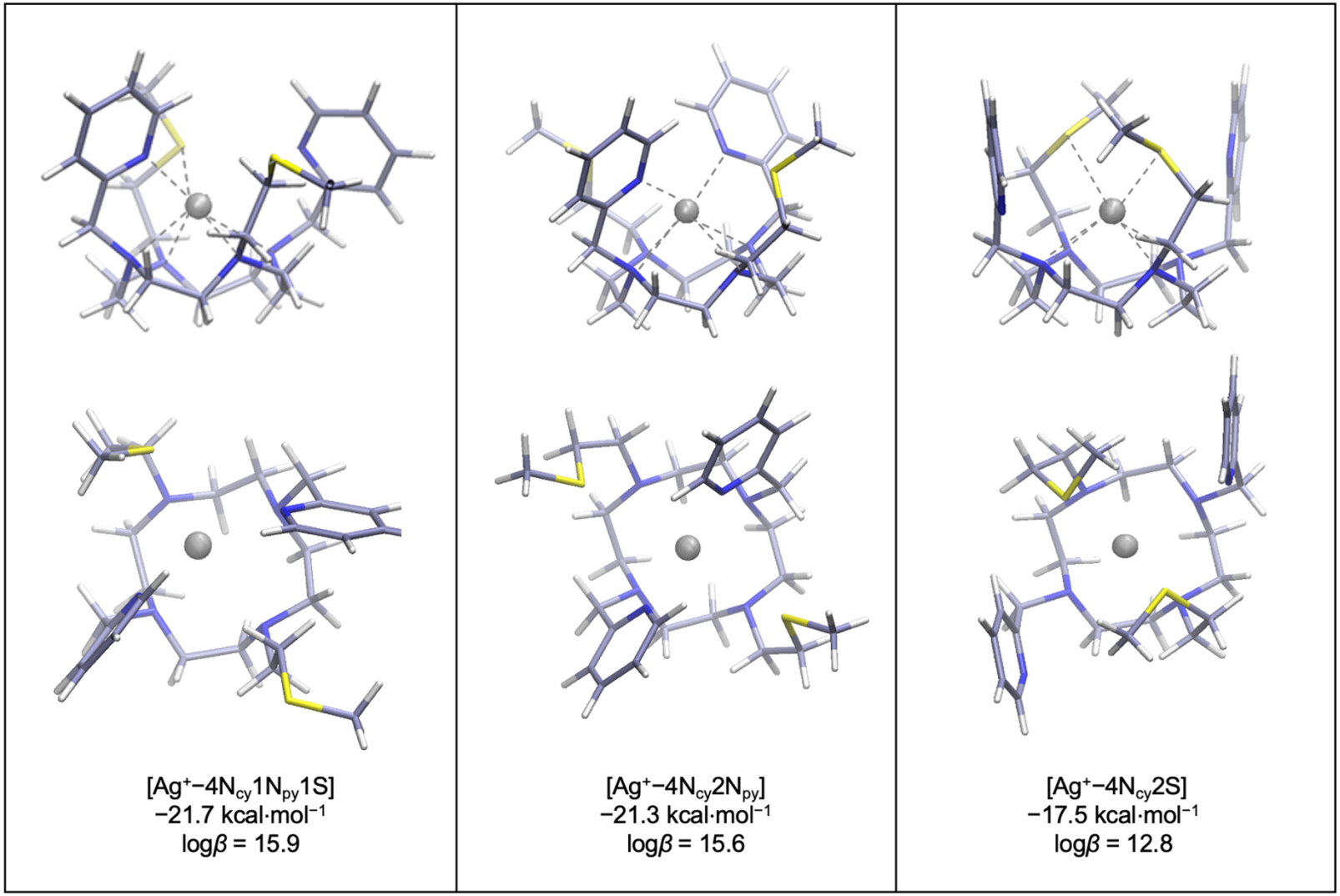

Figure S29. B3PW91 optimized geometrical structures of $[Ag(DO2S2Py)]^+$ calculated in water together with the relative binding energies ($kcal \cdot mol^{-1}$) and corresponding logβ values. Structures are displayed from multiple perspectives.

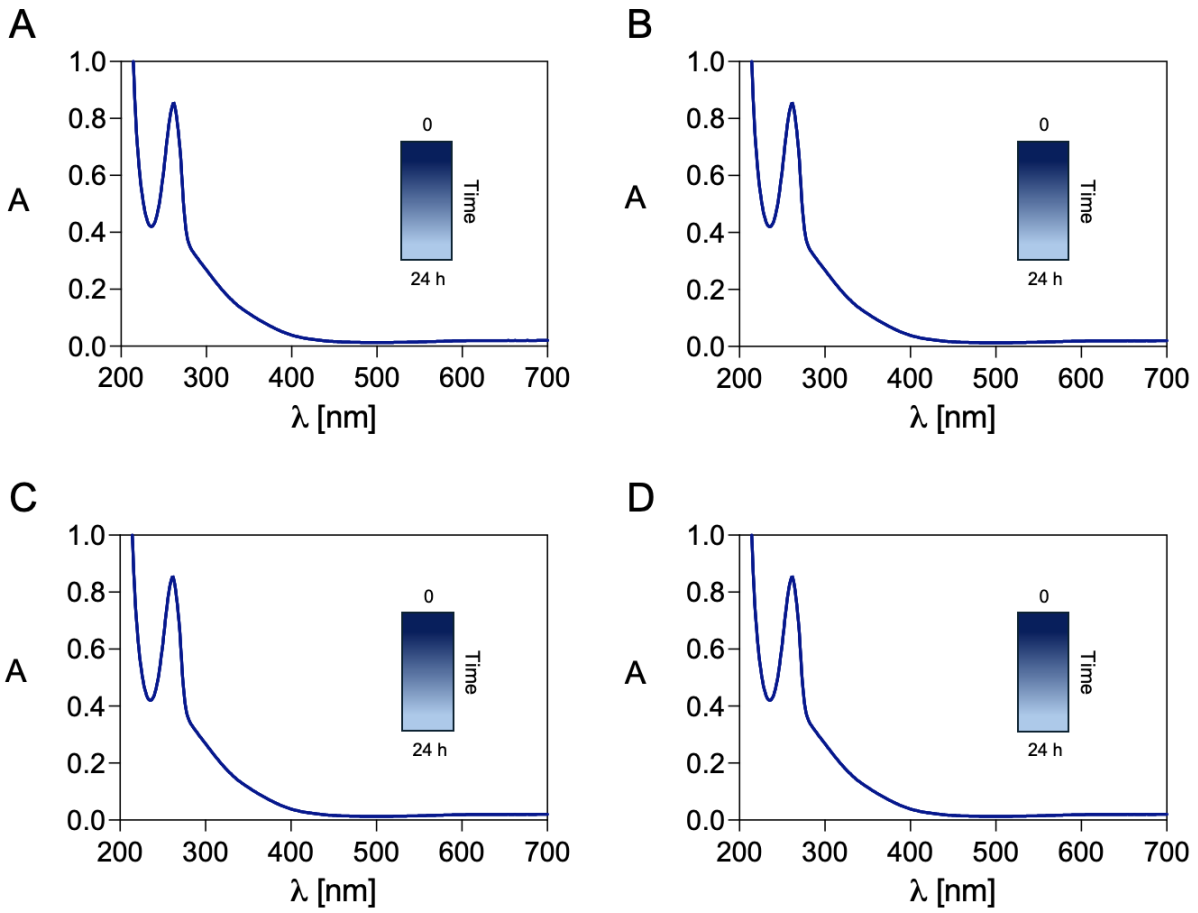

Figure S30. Representative time-dependent UV-Vis spectra of $[Cu(DO2S2Py)]^{2+}$ (T = 25°C, $C_{DO2S2Py}$ = C_{Cu} = $1 \cdot 10^{-4}$ M) in the presence of (A) Zn^{2+}, (B) Mg^{2+}, (C) Ca^{2+} ($C_{competitor}$ = $1 \cdot 10^{-3}$ M, $n_{competitor}/n_{complex}$ = 10) and (D) PBS (1:1 V/V dilution).

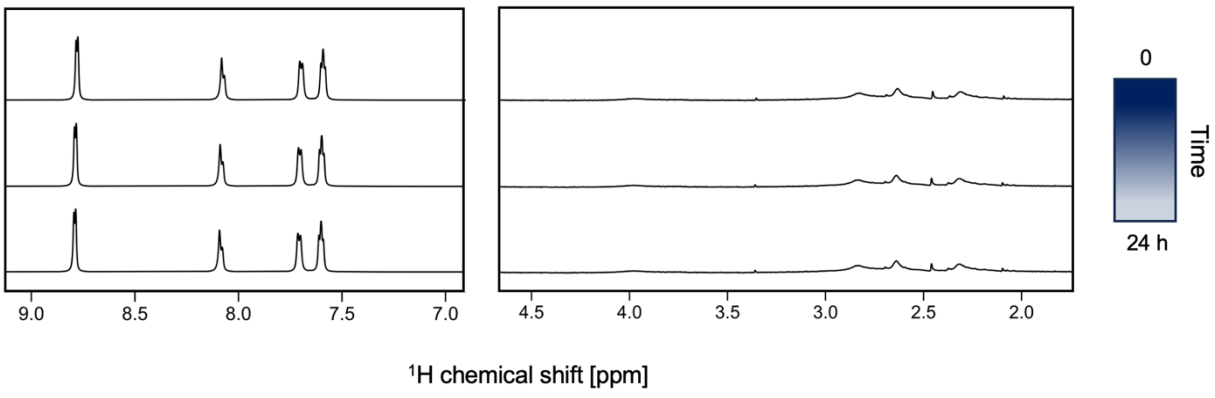

Figure S31. Representative time-dependent ^{1}H NMR spectra of $[Ag(DO2S2Py)]^{+}$ (400 MHz, T = 25°C, $C_{DO2S2Py}$ = C_{Ag} = $1 \cdot 10^{-3}$ M) in the presence of Zn^{2+} ($n_{Zn}/n_{complex}$ = 10). Identical spectra were obtained upon addition of Mg^{2+}, Ca^{2+} ($n_{competitor}/n_{complex}$ = 10) or PBS (1:1 V/V dilution), and therefore only representative data are shown.

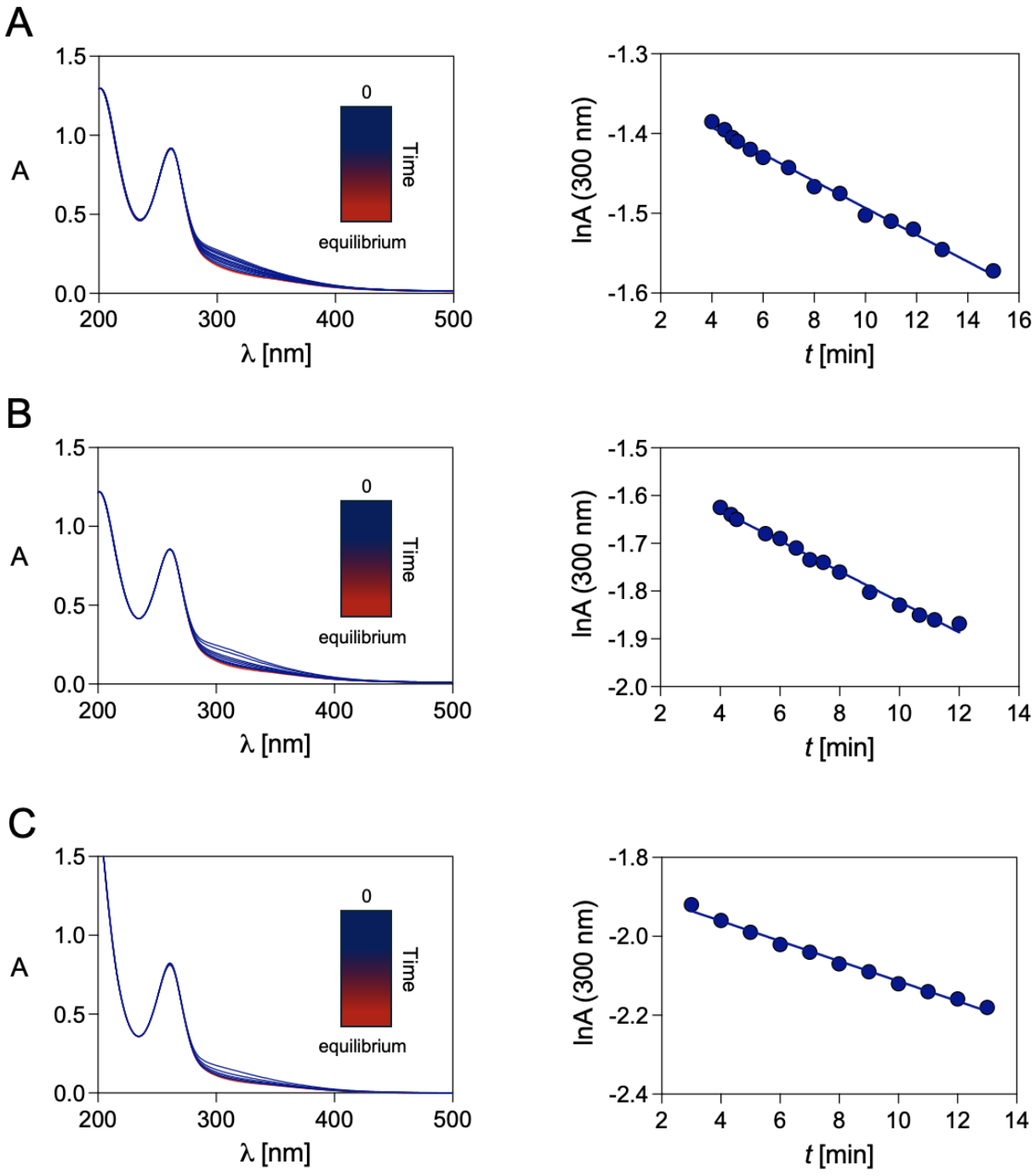

Figure S32. Left: UV-Vis spectra variation during the acid-assisted decomplexation assays for $[Cu(DO2S2Py)]^{2+}$ (C_{Cu} = $C_{DO2S2Py}$ = $1.0 \cdot 10^{-4}$ M) in (A) 0.4 M, (B) 0.6 M, (C) 0.8 M HCl solutions. Right: plot of ln*A* vs. *t* and the corresponding fitting line.

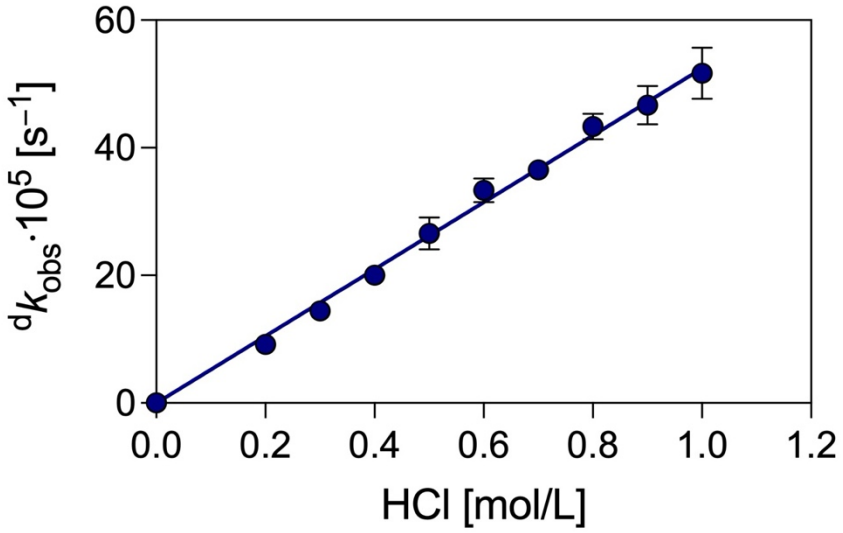

Figure S33. pH-Dependence of $^{d}k_{obs}$ for acid-mediated decomplexation of $[Cu(DO2S2Py)]^{2+}$ and the corresponding fitting line obtained with the equation $^{d}k_{obs} = {}^{d}k[H^{+}]$.

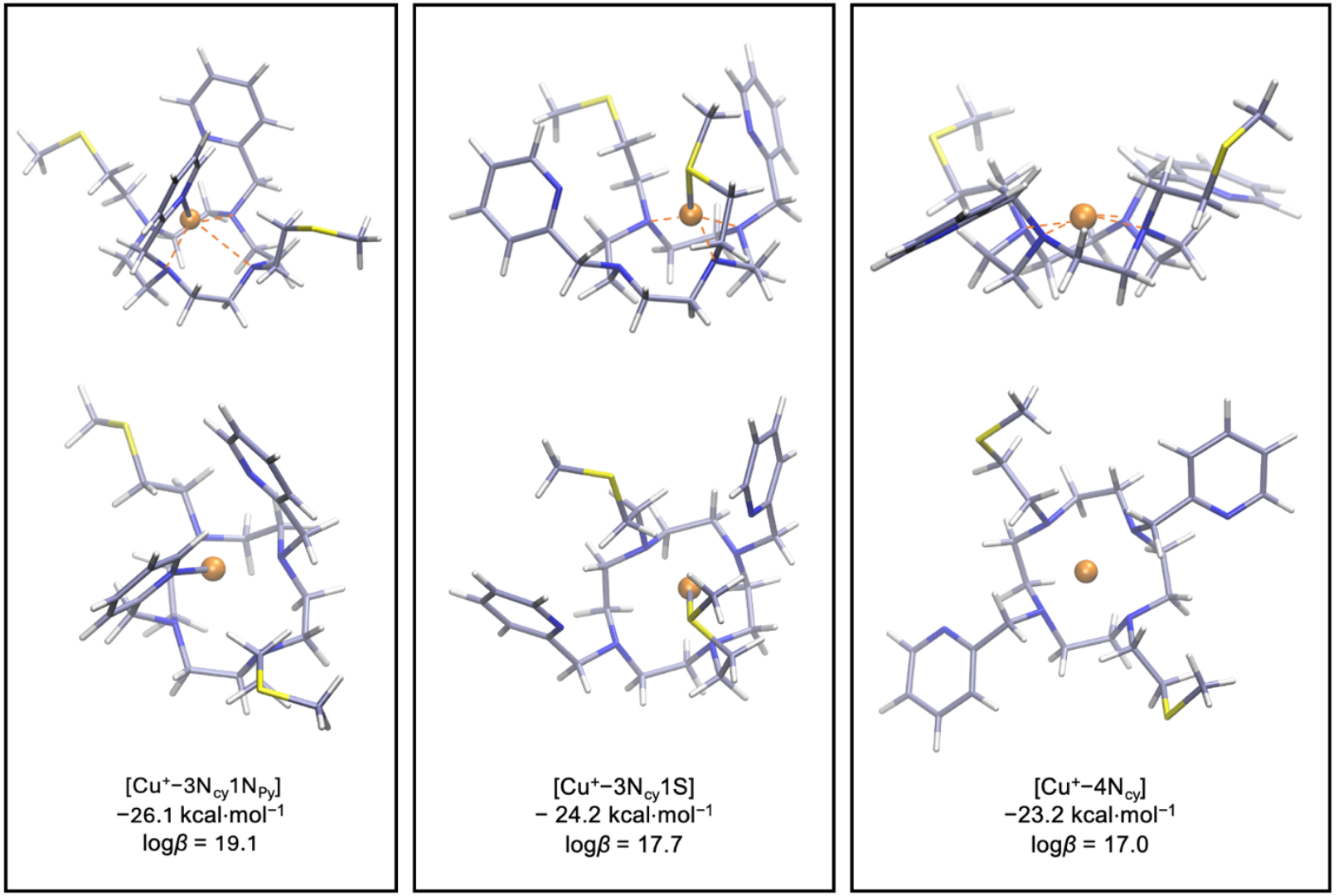

Figure S34. B3PW91 optimized geometrical structures of $[Cu(DO2S2Py)]^+$ calculated in water together with the relative binding energies (kcal·mol^{-1}) and corresponding logβ values. Structures are displayed from multiple perspectives.

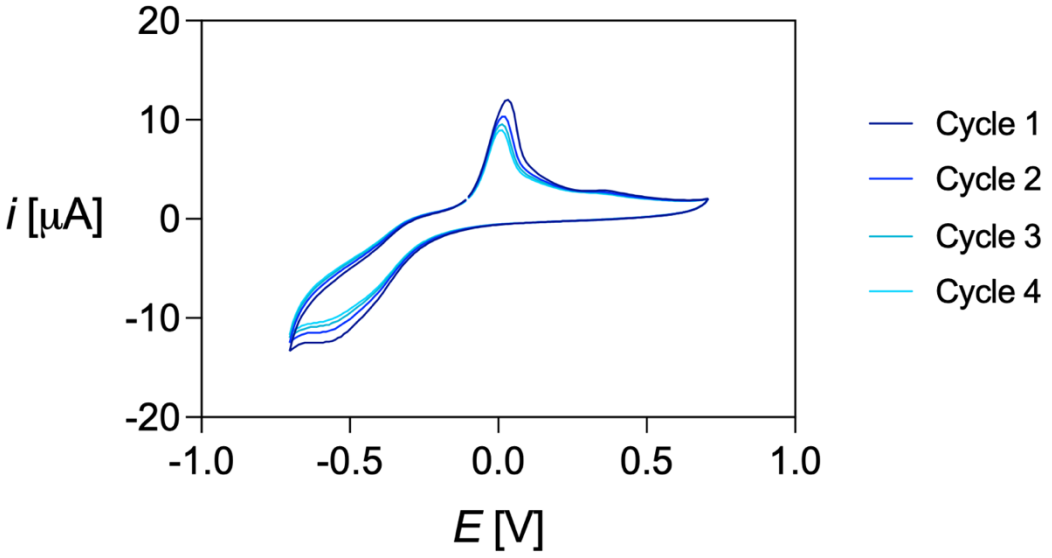

Figure S35. Representative cyclic voltammograms of $[Cu(DO2S2Py)]^{2+}$ (I = 0.15 M $NaNO_3$, T = 25°C, $C_{[Cu(DO2S2Py)]^{2+}} = 8 \cdot 10^{-4}$ M, pH = 7) acquired at a scan rate of 0.1 V/s.

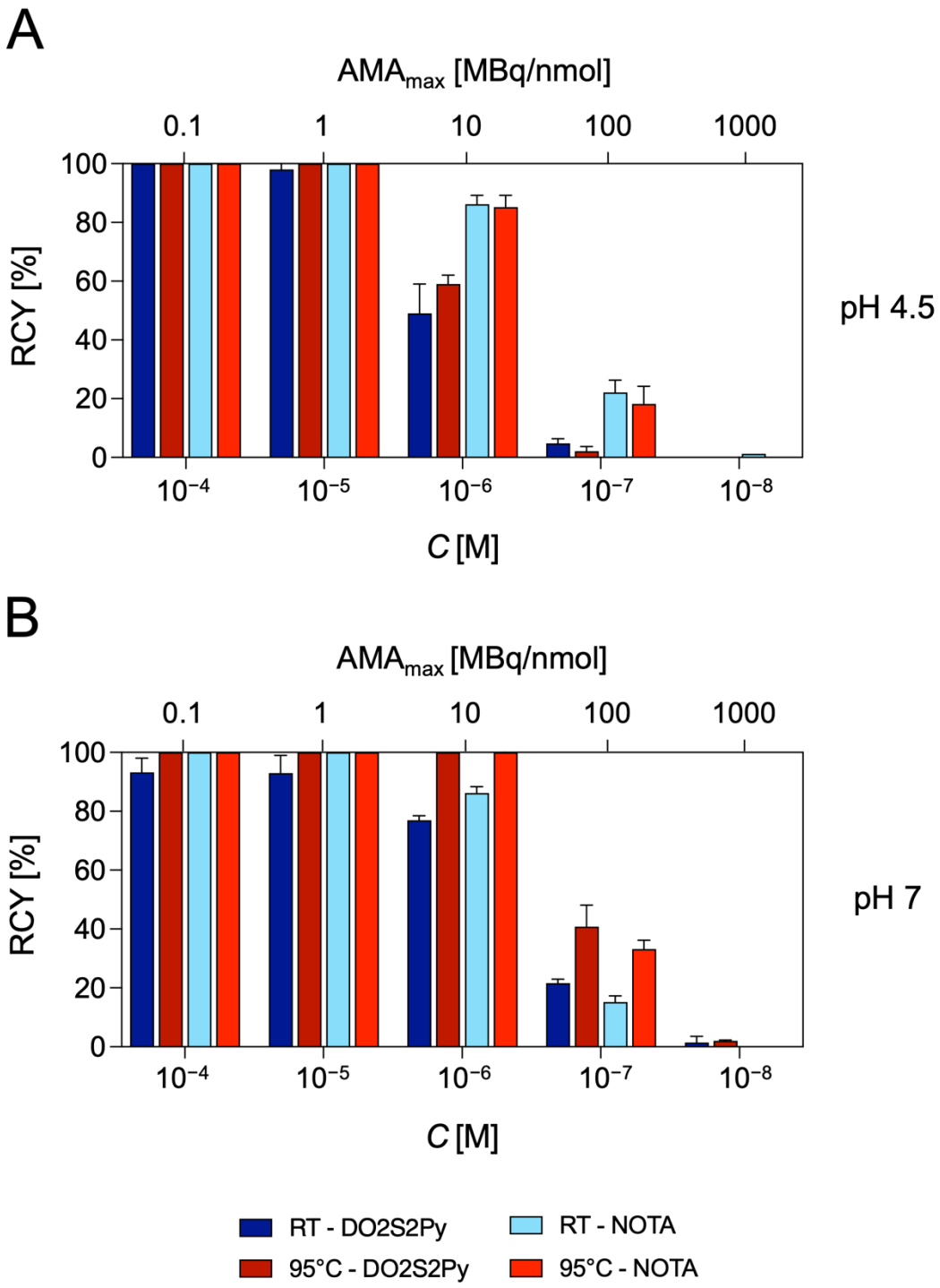

Figure S36. Concentration- and temperature-dependent [^{64}Cu]Cu^{2+} radiolabeling with DO2S2Py and NOTA at (A) pH 4.5 and (B) pH 7 (5 min reaction time).

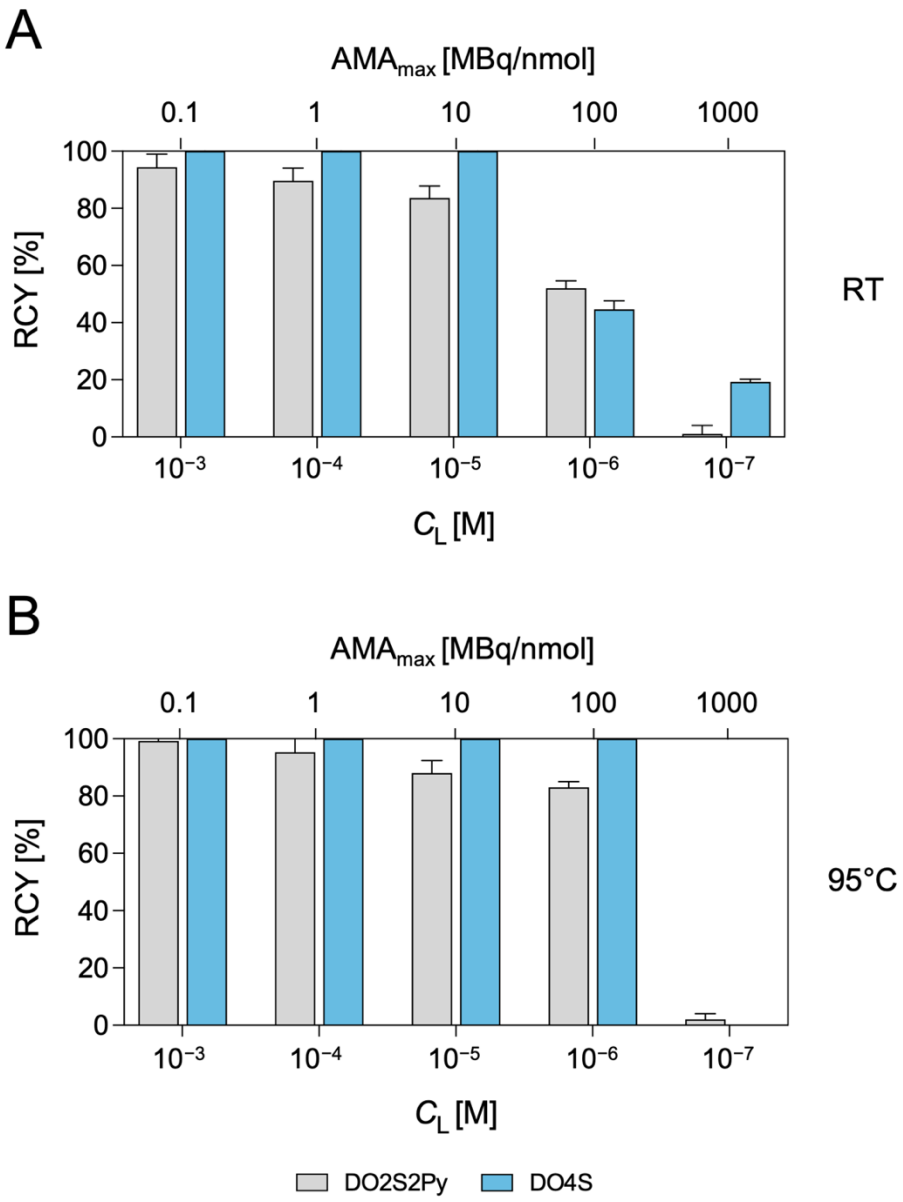

Figure S37. Concentration-dependent [^{111}Ag]Ag^{+} radiolabeling with DO2S2Py and DO4S (pH 7.4, 5 min reaction time) at (A) RT and (B) 95°C.

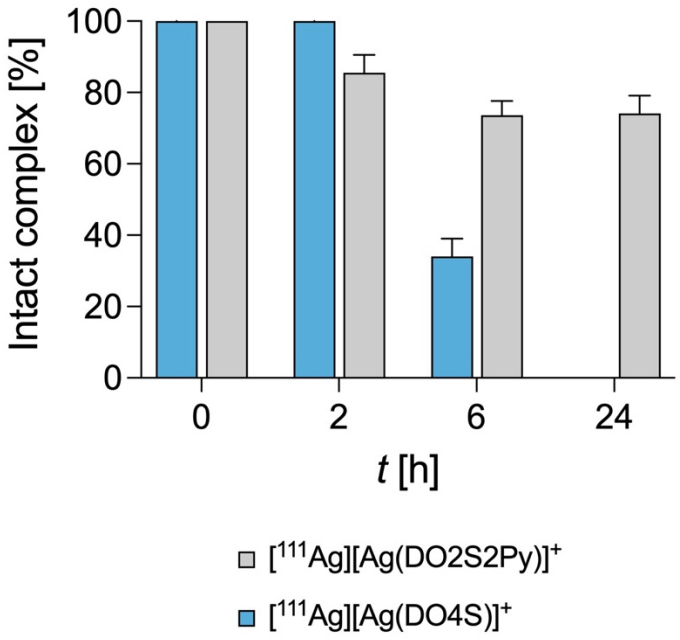

Figure S38. Comparison of the integrity of $[^{111}Ag][Ag(DO2S2Py)]^+$ and $[^{111}Ag][Ag(DO4S)]^+$ in human serum.

Supporting Tables

Table S1. Comparison of pK_a values of DO2S2Py, DO4S and pyridine-containing cyclen-based chelators.

	DO4S	DO2S2Py	Cyclen-Py [d]	Cyclen-2Py [e]	Cyclen-4Py [f]
pK_a	10.14	10.76 ± 0.03 [a] 10.8 ± 0.1 [b]	10.6	9.90	10.05
	7.29	7.75 ± 0.09 [a] 7.82 ± 0.05 [b] 7.78 ± 0.1 [c]	9.77	8.40	7.53
	1.9	3.10 ± 0.06 [a] 3.19 ± 0.05 [b] 3.33 ± 0.02 [c]	3.42	3.75	3.54
	-	2.6 ± 0.1 [a] 2.53 ± 0.02 [c]	< 3	2.50	2.23

a) Determined by pH-dependent ^{1}H NMR titrations.
b) Determined by pH-potentiometric titrations.
c) Determined by pH-dependent UV-Vis titrations.
d) Obtained from ref [3] (I = 1 M KNO_3).
e) Obtained from ref [4] (I = 0.10 M NMe_4NO_3).
f) Obtained from ref [5].

Table S2. Comparison of the approximate time required to reach equilibrium during the reaction between Cu^{2+} and different S-containing ligands (C_{Cu} = C_L = 1.0·10^{-4} M).[6]

pH	DO2S2Py	DO4S	DO3SAm	DO2A2S
2	< 10 sec	10 d	10 d	4 h
4.5/4.8	< 10 sec	50 min	60 min	< 10 sec
7	< 10 sec	< 10 sec	< 10 sec	< 10 sec

Table S3. EPR parameters obtained by the simulation of EPR spectra of $[Cu(DO2S2Py)]^{2+}$ in frozen solution. Coupling values are shown in 10^{-4} cm^{-1} values.

Complex	Anisotropic parameters [a]				Calculated [b]	Coordination	Ref.
	$g_\perp$	$g_\parallel$	$A_\perp$	$A_\parallel$	$g_{0,calc}$		
[Cu(DO2S2Py)]	2.067	2.248		144	2.127	$[4N_{cy}2N_{py}]$	This work
[Cu(DO2A2S]	2.075	2.272	24.5	142.8	2.141	$[2N,2O,2N_{ax}]$	7
$[Cu(DO3S)]^{2+}$ (1)	2.036	2.184	15.6	179.3	2.085	[4N]	7
$[Cu(DO3S)^{2+}$ (2)	2.048, 2.058	2.209	20.3, 23.5	171.2	2.105	$[4N,S_{ax}]$	7
$[Cu(Cpy_2)]$	2.07	2.19		193	2.11	$[4N,2N_{py}]$	4
$[Cu(CRpy_2)]$	2.05	2.22		140	2.11	$[2N,2N_{py},2N_{ax}]$	4

[a] The experimental errors were ± 0.002 for $g_\perp$ and ± 0.001 for $g_\parallel$, ± $2\cdot10^{-4}$ cm^{-1} for $A_\perp$ and ±$1\cdot10^{-4}$ cm^{-1} for $A_\parallel$.
[b] Calculated by the equation $g_{0,calc} = (2g_\perp+g_\parallel)/3$.

Table S4. Most relevant distances (Å) between the metal centers and the different coordinated atoms of the DO2S2Py ligand.

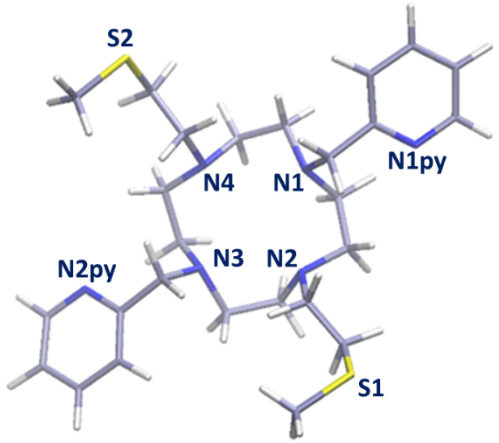

	$[Cu^{2+}–4N_{cy}2N_{py}]$	$[Cu^{2+}–4N_{cy}1N_{py}]$	$[Cu^{2+}–4N_{cy}1S]$	$[Cu^{2+}–4N_{cy}]$	$[Ag^{+}–3N_{cy}2Np_{y}1S]$	$[Ag^{+}–4N_{cy}2N_{py}]$	$[Ag^{+}–4N_{cy}2S]$	$[Cu^{+}–3N_{cy}1N_{py}]$	$[Cu^{+}–3N_{cy}1S]$	$[Cu^{+}–4N_{cy}]$
N1	**2.064**	**2.065**	**2.072**	**2.011**	**2.633**	**2.513**	**2.554**	**2.450**	**2.384**	**2.192**
N2	**2.291**	**2.104**	**2.087**	**2.026**	**2.586**	**2.812**	**2.725**	**2.167**	**2.251**	**2.230**
N3	**2.238**	**2.063**	**2.068**	**2.012**	2.997	**2.512**	**2.555**	2.668	2.797	**2.193**
N4	**3.158**	**2.121**	**2.098**	**2.023**	**2.613**	**2.826**	**2.669**	**2.300**	**2.148**	**2.235**
$N1_{py}$	**2.027**	**2.189**	5.149	4.963	**2.654**	**2.449**	4.870	**2.083**	4.310	5.167
$N2_{py}$	**2.000**	3.502	3.748	4.984	**2.591**	**2.446**	3.919	3.037	3.492	5.169
S1	4.049	5.340	**2.638**	5.748	**2.725**	3.795	**2.811**	5.494	**2.374**	5.889
S2	4.458	5.273	3.902	5.733	5.706	3.791	**2.768**	5.241	4.964	5.886

Table S5. Excitation energies Δ*E* (eV), absorption wavelength *λ* (nm), oscillator strength (*f*) and MO contribution % for selected transitions (Tr) of [Cu^{2+}−$4N_{cy}2N_{py}$] complex calculated by B3PW91

Tr[a]	Band	Δ*E*	*λ*	*f* (a)	MO contribution (b)
Tr1	I	1.93	641	0.0006	H-13_β → L_β 33% H-9_ β→ L_ β 15%
Tr2	II	3.86	321	0.0184	H-3_ β→ L_ β 15%
Tr3		4.13	300	0.0281	H-6_ β→ L_ β 22%
Tr4		4.41	281	0.0955	H-7_ β→ L_ β 41% H-10_ β→ L_ β 18%
Tr5	III	4.81	258	0.0183	H-4_α→ L+1_ α 41%, H-3_ β→ L+2_ β 22%
Tr6		5.24	237	0.0654	H-5_α→ L_α 33% H-4_ β→ L+1_ β 28%
Tr7		5.34	232	0.0187	H-5_ α→ L+1_ α 18% H-6_ β→ L+1_ β 13%
Tr8		5.41	229	0.0250	H-17_ β → L_ β 46%
Tr9		5.49	226	0.0207	H-6_ α → L+1_ α 20%, H-3_ β → L+4_ β 34%
Tr10		5.51	225	0.0022	H-15_ β → L_ β 40% H-14_ β→ L_ β 25%

Tr = transition number.
(a) Only vertical transitions with oscillator strength greater than 0.0180 are reported, except for the most red-shifted transition (Tr1).
(b) Only contributions larger than 15% are reported.
functional.

Table S6. Comparison of the acid decomplexation half-life ($^{d}t_{1/2}$) of the Cu^{2+} complexes of DO2S2Py and other S-containing chelators (^{d}k, $^{d}k_2$ determined by fitting the experimental data with the equation $^{d}k_{obs} = {}^{d}k[H^+]$ for DO2S2Py, DO4S, DO2A2S, and TE4S or $^{d}k_{obs} = {}^{d}k\,[H^+] + {}^{d}k_2\,[H^+]^2$ for TRI4S).[6]

[HCl] [M]	**$^{d}t_{1/2}$**				
	DO4S [min]	**DO2A2S [h]**	**TRI4S [min]**	**TE4S [min]**	**DO2S2Py [min]**
0.1	254	17.8	50.4	1.0	141.5
0.2	118	8.8	3.8	0.9	80.1
0.4	58.3	4.0	1.4	0.7	43.5
0.6	35.3	2.9	0.6		31.7
0.8	25.5	2.3	0.4	< 30 sec	26.7
1.0	19.4	1.8	0.3		22.4
^{d}k [$M^{-1}\cdot s^{-1}$]	$(5.7 \pm 0.1)\cdot 10^{-4}$	$(1.04 \pm 0.02)\cdot 10^{-4}$	$(1.7 \pm 0.6)\cdot 10^{-2}$	$\sim 10^{-2}$	$(5.32 \pm 0.05)\cdot 10^{-4}$
$^{d}k_2$ [$M^{-1}\cdot s^{-1}$]	-	-	$(1.9 \pm 0.7)\cdot 10^{-2}$	-	-

References

1 M. Tosato, M. Asti, M. Dalla Tiezza, L. Orian, D. Häussinger, R. Vogel, U. Köster, M. Jensen, A. Andrighetto, P. Pastore and V. Di Marco, *Inorg. Chem.*, 2020, **59**, 10907–10919.

2 M. Tosato, S. Franchi, M. Dalla Tiezza, L. Orian, T. Gyr, A. Alker, G. Zanoni, P. Pastore, A. Andrighetto, U. Köster, M. Jensen, H. Mäcke, M. Asti and V. Di Marco, *Inorg. Chem.*, 2023, **62**, 20777–20790.

3 S. El Ghachtouli, C. Cadiou, I. Déchamps-Olivier, F. Chuburu, M. Aplincourt and T. Roisnel, *Eur. J. Inorg. Chem.*, 2006, **2006**, 3472–3481.

4 N. Bernier, J. Costa, R. Delgado, V. Félix, G. Royal and R. Tripier, *Dalton Trans.*, 2011, **40**, 4514–4526.

5 B. L. McNeil, K. J. Kadassery, A. W. McDonagh, W. Zhou, P. Schaffer, J. J. Wilson and C. F. Ramogida, *Inorg. Chem.*, 2022, **61**, 9638–9649.

6 M. Tosato, M. Pelosato, S. Franchi, A. A. Isse, N. V. May, G. Zanoni, F. Mancin, P. Pastore, D. Badocco, M. Asti and V. Di Marco, *New J Chem*, 2022, **46**, 10012–10025.

7 M. Tosato, M. Dalla Tiezza, N. V. May, A. A. Isse, S. Nardella, L. Orian, M. Verona, C. Vaccarin, A. Alker, H. Mäcke, P. Pastore and V. Di Marco, *Inorg. Chem.*, 2021, **60**, 11530–11547.